This is the peer reviewed author accepted manuscript (post print) version of a published work that appeared in final form in:

Li, Lin, Xue, Chaorui, Chang, Qing, Ren, Xiaohu, Li, Ning, Yang, Jinlong, Hu, Shengliang, Xu, Haolan 2024 'Polyelectrolyte hydrogel-functionalized photothermal sponge enables simultaneously continuous solar desalination and electricity generation without salt accumulation', Advanced Materials, online, pp. 1-12

This un-copyedited output may not exactly replicate the final published authoritative version for which the publisher owns copyright. It is not the copy of record. This output may be used for non-commercial purposes.

The final definitive published version (version of record) is available at:
https://doi.org/10.1002/adma.202401171

Persistent link to the UniSA Research Outputs Repository:
https://researchoutputs.unisa.edu.au/11541.2/38270

General Rights

Copyright and moral rights for the publications made accessible in the UniSA Research Outputs Repository are retained by the authors and/or other copyright owners and it is a condition of accessing publications that users recognize and abide by the legal requirements associated with these rights.

- Users may download and print one copy for the purpose of private study or research.
- You may not further distribute the material or use it for any profit-making activity or commercial gain
- You may freely distribute the persistent link identifying the publication in the UniSA Research Outputs Repository

If you believe that this document breaches copyright, please contact us and provide details. We will remove access to the work immediately and investigate your claim.

Polyelectrolyte Hydrogel-Functionalized Photothermal Sponge Enables Simultaneously Continuous Solar Desalination and Electricity Generation without Salt Accumulation

Lin Li, Chaorui Xue, Qing Chang, Xiaohu Ren, Jinlong Yang, Shengliang Hu and Haolan Xu**

L. Li, Dr. C. Xue, Prof. Q. Chang, Prof. J. Yang, Prof. S. Hu
Research Group of New Energy Materials and Devices
State Key Laboratory of Coal and CBM Co-Mining
North University of China
Taiyuan 030051, P. R. China.
*Corresponding Author, E-mail: hsliang@yeah.net
Prof. J. Yang
State Key Laboratory of New Ceramics and Fine Processing
Tsinghua University
Beijing 100084, P. R. China.
Prof. X. R
College of Materials Science and Engineering, Xi'an University of Architecture and Technology, Xi'an 710055, P. R. China.
Prof. X. R, Prof. H. Xu
Future Industries Institute, UniSA STEM
University of South Australia
Adelaide, South Australia, Australia
E-mail: haolan.xu@unisa.edu.au

Keywords: solar evaporation, carbon dots-modified graphene, desalination, evaporation-electricity generator, self-regeneration

Technologies that can simultaneously generate electricity and desalinate seawater are highly attractive and required to meet the increasing global demand for power and clean water. Here we develop a bifunctional solar evaporator that features continuous electric generation in seawater without salt accumulation by rational design of polyelectrolyte hydrogel-functionalized photothermal sponge. This evaporator not only exhibits an unprecedentedly high water evaporation rate of 3.53 $kg•m^{-2}•h^{-1}$along with 98.6% solar energy conversion

efficiency, but also can uninterruptedly deliver a voltage output of 0.972 V and a current density of 172.38 μA•cm^{-2} in high-concentration brine over a prolonged period under one sun irradiation. Many common electronic devices can be driven by simply connecting evaporator units in series or in parallel without any other auxiliaries. Different from the previously proposed power generation mechanism, our study reveals that the water-enabled proton concentration fields in intermediate water region can also induce an additional ion electric field in free water region containing solute to further enhance electricity output. Given the low-cost materials, simple self-regeneration design, scalable fabrication processes and stable performance, this work offers a promising strategy for addressing the shortages of clean water and sustainable electricity.

1. Introduction

Along with the world climate change, economic development and population growth, many countries are suffering from a severe scarcity of natural freshwater resources and sustainable electricity [1-2]. Solar-driven seawater evaporation for parallel clean water and electricity generation is an ideal solution to address these impending issues simultaneously, as solar energy is an inexhaustible energy source and the oceans represent the largest water reservoir on Earth [3]. In recent years, the concept of solar-driven interfacial water evaporation with extremely high energy efficiencies has been extensively explored for acquiring clean water from seawater or sewage [4-5]. This cost-effective technique offers all-in-one solutions where multiple functions including sunlight harvesting, solar-to-heat conversion, liquid wicking, water flow regulation and self-floating are integrated into a single system [6]. Since there is no thermodynamic limit on the quantity of photon that is able to be absorbed by a photothermal material, over 99% of the sunlight reaching the photothermal material can be utilized directly for thermal generation [7-8]. Therefore, near 100% solar-to-steam conversion efficiency could be realized thanks to this high photothermal conversion, as well as minimized heat losses to the environment and bulk water [9].

In addition to rational energy management, reducing water evaporation enthalpy via elaborately designed hydrogels can unprecedentedly elevate the solar-to-steam generation performance with the same solar energy input [10]. Hydrophilic functional groups in hydrogels can trap water molecules via hydrogen bonds to tune water states and phase transition behaviors [11]. By tailoring building blocks in hydrogels such as functional groups/additives, polymer/monomer backbones, and cross-linkers, a higher content of intermediate water that possesses a lower evaporation enthalpy than free water and bound water is able to be

produced in hydrogel networks, resulting in faster evaporation under natural sunlight. However, the existing hydrogel-based materials possess poor stretchability and are easily destroyed during deformation [12]. To facilitate the practical applications of these hydrogels, mechanical properties and scalability as well as the simplicity of preparation methods need to be remarkably improved. In addition, rendering the hydrogels extra functions such as power generation during interfacial solar evaporation could open new avenues for diverse and attractive applications [13-14].

As interfacial solar evaporation involves water evaporation, vaporization-induced electricity generation systems can be created and incorporated into solar interfacial evaporation systems [15]. For instance, the thermal energy generated during the solar evaporation processes can be utilized directly and indirectly for power generation via pyroelectric, piezoelectric and triboelectric effects [16-18]. Unfortunately, these techniques have their own limitations from power generation capacity and unsustainable electricity output. Another new technology of electricity generation along with water vaporization takes advantage of an evaporation-induced salinity gradient by means of ion selective through membranes [19]. However, its evaporation rate is only 1.1 kg m^{-2} h^{-1} along with a ~75% of solar thermal efficiency. Besides, hydrovoltaic technologies based on evaporation-driven water flow inside nanochannels can induce a carrier concentration gradient to yield sustained electricity, whereas it is not able to simultaneously produce considerable clean water owing to the limitation of water supply for hydrovoltaic processes [15, 20-21]. Therefore, it is imperative to develop new strategies for juggling rapid water evaporation and continuous electricity generation from interfacial solar evaporation of seawater or wastewater. To realize this, elaborate design and fabrication of multifunctional photothermal materials/hydrogels are vitally important.

Graphene-based material displays superiority in broad-band absorption from the visible to infrared range and excellent stability, which makes it an appealing candidate as the desirable solar absorber. However, graphene as a photothermal material usually confronts the problem of high emissivity in the infrared range, leading to huge heat radiation loss and remarkable reduction in the overall photothermal efficiency [22]. Carbon dots (CDs), as a representative carbon fluorescent material, possess molecular-like behavior and delocalized electronic structure [23]. Loading CDs on graphene-based materials not only suppresses infrared emissivity of graphene [8], but also provides more hydrophilic functional groups for water activation. Therefore, it is expected to achieve higher solar-to-heat conversion efficiency and faster water evaporation rate over graphene-CDs hybrids.

Recently, through control of the directional flow of water and inhomogeneous distribution of water molecules in the polyelectrolyte membranes, oriented proton movement can be induced that endows high-voltage output under proper humidity [24-25]. However, after a long period of water feeding, the inhomogeneity of water molecules distribution within the membrane significantly reduces the electricity output [26]. This means that its power output can be hardly sustained without attenuation. To tackle this problem, here we present a self-sustained proton concentration gradient in the polyelectrolyte membrane driven by solar interfacial water evaporation for achieving persistent power generation. Our solar evaporation-electricity generation system is constructed using the commercial melamine sponge (MS) functionalized by CDs-coupled graphene and polyelectrolyte hydrogels without the need for tedious, stringent or costly fabrication steps, showing favorable mechanical flexibility and excellent scalability. It can persistently deliver not only a voltage of up to 0.85 V cm^{-2} but also an ultrafast evaporation rate of 3.53 $kg•m^{-2}•h^{-1}$ with a 98.6% solar-to-vapor energy conversion efficiency under one sun irradiation. More impressively, we found that the univalent cations and polyvalent anions in brine can significantly boost the electricity output, acquiring a maximum open-circuit voltage of up to 1.44 V and a short-circuit current of up to 0.37 mA for a 1 cm^2 unit, without the burden of salt accumulation on the evaporation surface of the system. By simply connecting units in parallel and in series without any other auxiliaries, the presented system sufficiently powers up many common electronics. This study offers a strategy for durable power generation and highly efficient water purification at the same time.

2. Results and Discussion

2.1. Fabrication and Characterization of the Electricity-Generation Evaporator

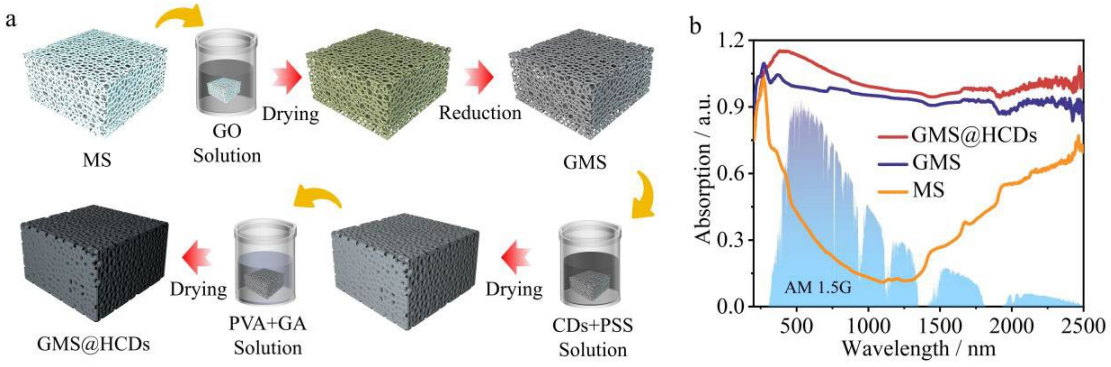


Figure 1. Preparation processes and optical absorption of samples. **a**) Schematic illustration of GMS@HCDs; **b**) UV-vis-NIR absorption spectra of MS, GMS and GMS@HCDs

As illustrated in Figure 1a, commercial MS was firstly coated with reduced graphene

oxides (rGO), which endowed the MS with certain electrical conductivity as well as superior solar light harvesting and conversion functions. The resultant rGO-coated MS (labeled as GMS) was then filled with a mixed solution containing polystyrene sulfonic acid (PSS) and coal-pitch-based CDs which can further improve sunlight conversion and utilization. After drying, an aqueous solution of polyvinyl alcohol (PVA) and glutaraldehyde (GA) was uniformly spread on the top surface to form a gel. The obtained sample was immersed into deionized (DI) water overnight to remove free chemicals and materials. After that it was frozen at around -18 ºC and then thawed in DI water at room temperature to obtain the electricity-generation evaporator, named GMS@HCDs. After a series of treatments, the color of MS was changed from white to black (**Figure S1, Supporting Information**). The as-prepared GMS@HCDs can float on water surfaces (**Figure S2, Supporting Information**).

Scanning electron microscopy (SEM) images of GMS showed that the open porous structures of the MS (**Figure S3a-c, Supporting Information**) were still present as shown in **Figure S3d-f, Supporting Information**. Many observed tiny sheets on the skeletons of MS revealed the formation of the rGO coating layers, which was further confirmed by X-ray diffraction (XRD) characterization (**Figure S4, Supporting Information**). In the GMS@HCDs, one can clearly observe that the hydrogels of PSS and PVA occupied most of the pore space of the GMS (**Figure S3g-i, Supporting Information**), leaving behind a large number of much smaller holes. This change in porous structures may enhance capillary force [20], and thereby the water absorption properties of GMS@HCDs are superior to the primary MS (**Figure S5, Supporting Information**). Fourier-Transform infrared (FTIR) spectrum of GMS@HCDs showed strong absorption signals at 1650, 1150, 1029, and 1005 cm^{-1} (**Figure S6, Supporting Information**), which can be attributed to the C=C stretching in the aromatic rings and C–O stretching [26], S=O and S-OH stretching of $-SO_3H$ groups [27], respectively. This result proved that GMS@HCDs contained characteristic peaks of PVA and PSS and abundant hydrophilic groups. By electrochemical impedance spectroscopy (EIS) characterizations (**Figure S7, Supporting Information**), the introduction of CDs and hydrogel can reduce the interfacial impedance of GMS and MS, benefiting charge migration. When a voltage was applied on the two sides of the monolith of GMS and GMS@HCDs, the light-emitting diode (LED) lamp between them was lightened, indicating their good electrical conductivity (**Figure S8, Supporting Information**). In addition, the ultraviolet–visible-near-infrared (UV–Vis-NIR) spectra (**Figure 1b**) of the GMS@HCDs showed an excellent absorption feature throughout the sunlight spectrum, significantly higher that of the original MS. Therefore, the obtained GMS@HCDs possessed both excellent light absorption and

electrical conductivity which were conducive to simultaneous efficient interfacial solar evaporation and power generation.

2.2 Solar Interfacial Water Evaporation Performance

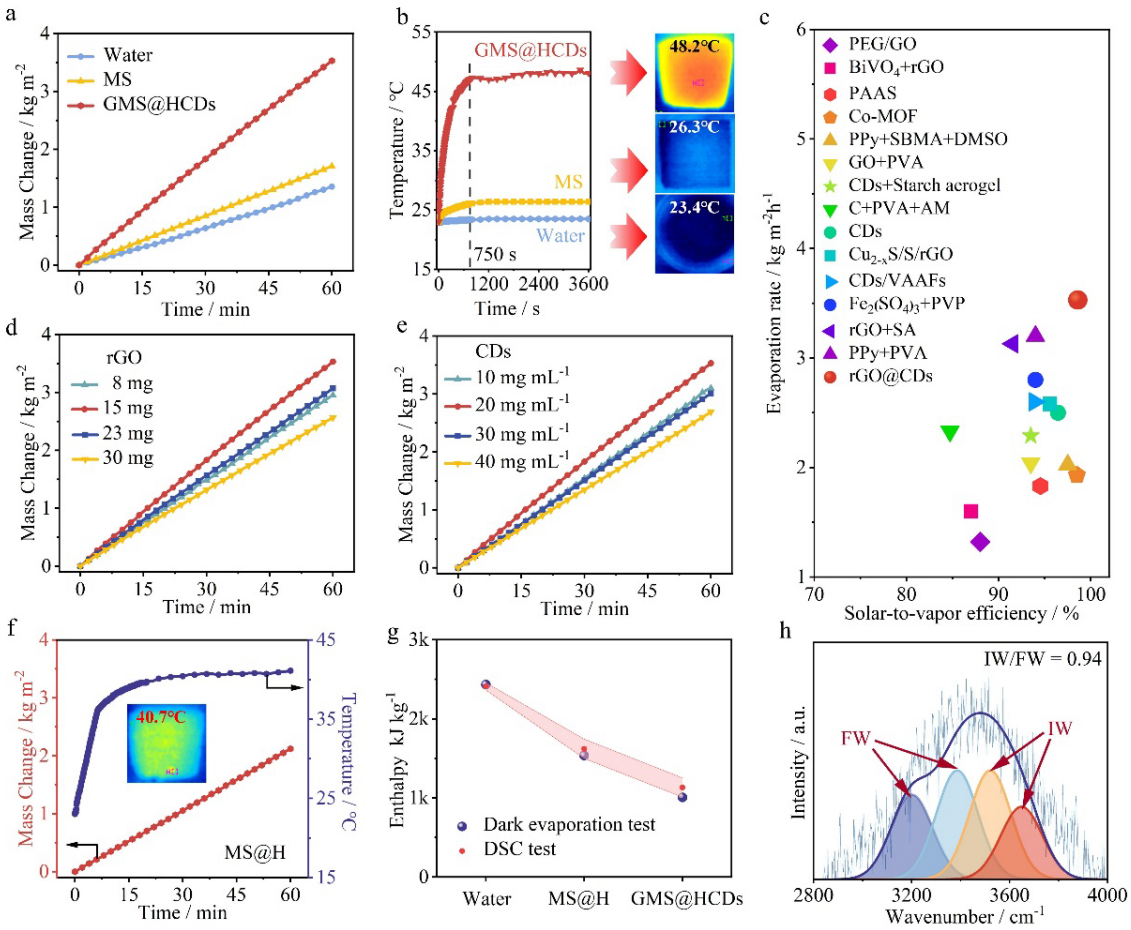


Figure 2. Solar interfacial evaporation performance. **a**) Mass change of water evaporation over time under one sun; **b**) Surface temperatures of the different evaporation systems and bulk water vs. irradiation time (Left) and corresponding infrared photographs (Right) under one sun; **c)** Comparisons of water evaporation rate and solar-to-steam efficiency from GMS@HCDs with reported evaporators under one sun; **d**) The effect of rGO mass on the evaporation performance of GMS@HCDs without changing CDs content; **e**) The influence of CDs concentration for preparing GMS@HCDs on its evaporation performance; **f)** The changes of water evaporation mass and surface temperature over time for MS@H under one sun; **g**) Water vaporization enthalpy values obtained by dark experiment and measured by DSC; **h**) Raman spectra displaying the fitting peaks representing IW and FW in the GMS@HCDs.

To assess the solar evaporation performance, the overall mass change with and without

GMS@HCDs under one sun (1 kW m^{-2}) irradiation was recorded. As shown in **Figure 2a**, the steam generation with the GMS@HCDs was much faster than that of the MS and water without the evaporator. An extremely high evaporation rate of 3.53 kg m^{-2} h^{-1} was achieved for GMS@HCDs, which was 2.6 times of that for pure water. **Figure 2b** (left) illustrated the surface temperatures of GMS@HCDs and the water without GMS@HCDs relative to irradiation time. Upon illumination, the surface temperature of the GMS@HCDs increased from 22.5 to 47.5 °C within 750 s, and then reached the plateau region (~48.2 °C), which indicated an energy balance of light-to-heat conversion and evaporation consumption. In contrast, the MS and bulk water showed much lower steady temperature of 26.3 and 23.4 °C, respectively, even after 1 h due to the poor light absorption of pristine MS and water. These results verified the excellent solar-thermal energy conversion and heat localization of the GMS@HCDs.

The corresponding thermal conversion efficiency (η) for solar-to-steam generation was then assessed by the following formula [6],

$$\eta = \frac{\dot{m} H_e}{C_{opt} q_0} \quad (1)$$

where ṁ, C_{opt}, q_0 represent the evaporation rate, optical concentration, solar irradiation intensity, respectively. H_e is the evaporation enthalpy of the water in the evaporator which can be measured and calculated by the following equation [28]:

$$H_e m_e = H_0 m_0 \quad (2)$$

where H_0, m_0 refer to the evaporation enthalpy, the evaporation rate of bulk water, and m_e is the evaporation rate of the evaporator (i.e., GMS@HCDs) in dark conditions, respectively. They can be tested under the same conditions as shown in Supplementary Fig. 5. According to the obtained H_e value of GMS@HCDs, the solar-to-vapour conversion efficiency was calculated to be 98.6% under one sun (**Figure 2c** and **Table S1, Supporting Information**). So far, there are few solar evaporators reported previously had such excellent evaporation performances [10, 28-40].

2.3 Reasons for High-Efficiency Solar Interfacial Evaporation

The superior water evaporation performance of the GMS@HCDs should be intimately related to its material composition and microstructure. To investigate the effect of photothermal materials, we initially controlled the content of rGO in GMS@HCDs without changing other parameters, and then measured their evaporation rate under one sun irradiation. As shown in **Figure 2d**, the optimum loading amount of rGO is 15 mg for the MS with a dimension of 20 mm×20 mm×7.5 mm. Further increase in rGO amount led to a decrease in evaporation rate. Similarly, it was found that the optimal content of CDs was 20 mg, while

excessive CDs also gave rise to decreased evaporation performance (**Figure 2e**). To identify the roles of the hybrid hydrogels of PSS and PVA, we further fabricated another control sample (labeled as MS@H) without CDs and rGO and replaced GMS with MS. Unexpectedly, the MS@H still displayed a high evaporation rate of 2.1 kg m^{-2} h^{-1} under one sun (**Figure 2f**). This anomalous phenomenon should be associated with hydrogel-enabled reduction in vaporization enthalpy by increasing the content of intermediate water (IW) [10].

To verify water activation in GMS@HCDs, we further tested the vaporization enthalpy of the water and the content of IW hosted in GMS@HCDs based on the equation (2) and by the DSC [41] (**Figure S9, Supporting Information**). The results are well consistent (Figure 2g). Impressively, the vaporization enthalpy of water in GMS@HCDs is around 1,005 kJ kg^{-1}, which is about 41.3% of that of bulk water (2,432 kJ kg^{-1}). Similarly, since the CDs and rGO contain abundant hydrophilic groups (e.g. –COOH, -OH), they should also be able to induce higher proportion of IW and further reduce the vaporization enthalpy of water in GMS@HCDs compared to MS@H. According to the Raman spectra in the region of O-H stretching, the ratio of IW to free water (FW) of the water in the GMS@HCDs was 0.94 (**Figure 2h**), which was much higher than that of water in GMS (0.41, **Figure S10, Supporting Information**). This suggests that both hydrogel (i.e., PSS and PVA) and photothermal materials (i.e., rGO and CDs) in GMS@HCDs favor the formation of IW. Besides, the contents of IW in GMS@HCDs can be tailored by adjusting the proportion of PSS and PVA in hydrogels, leading to the variation in solar evaporation performance (**Figure S11, Supporting Information**).

2.4 Salt-Rejecting Function and Durability in Brine

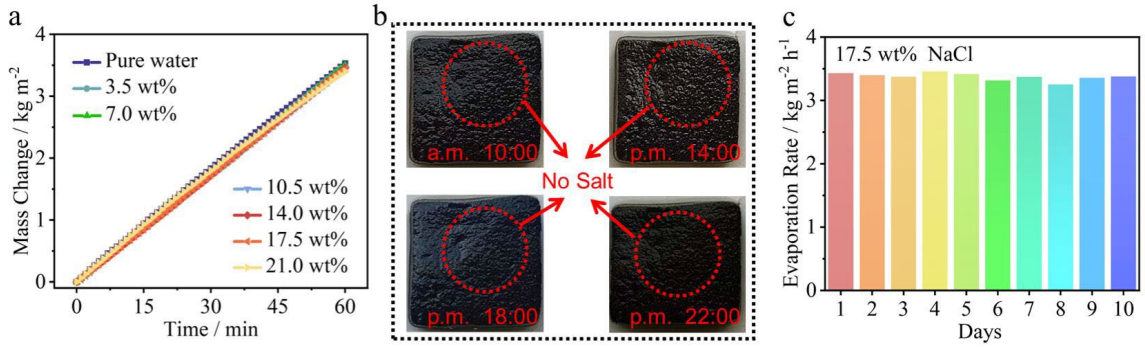


Figure 3. Salt-rejecting function and durability in brine. **a**) The evaporation performance of GMS@HCDs in wide ranges of salinity; **b**) Typical photographs of GMS@HCDs exposed for continuous 10 h in 17.5 wt% NaCl solution under natural sunlight irradiance; **c**) The durability of GMS@HCDs in 17.5 wt% NaCl brine.

The salt-rejecting performance of GMS@HCDs was evaluated in synthetic seawater solution (i.e., NaCl solution) with salinity ranges from 0 to 21wt% (**Figure 3a**). It manifests stable evaporation efficiency in different concentrations of NaCl solution due to the presence of hydrogel coats, which possesses an intrinsic anti-salt-fouling ability by establishing an equilibrium between water transport-induced salt ion absorption and diffusion-enabled salt ion discharge [42-43]. No salt formation was observed on the surface of GMS@HCDs after more than 10 h continuous testing with 17.5 wt% NaCl solution under natural sunlight irradiation (**Figure 3b**), confirming its excellent self-regeneration function. Moreover, when solid salts were added directly on the top surface of GMS@HCDs, they gradually dissolved back to the bulk NaCl solution after merely 3 h under light irradiation (**Figure S12, Supporting Information**). The rapid diffusion and convection between the top surface and the bulk salt solution underneath can significantly avoid the formation of hypersaline solution on the evaporation surfaces, contributing the salt-rejecting function of GMS@HCDs. In addition, the mechanical stability of the salt-rejecting GMS@HCDs was examined by soaking it in 17.5 wt% NaCl solution for 10 days under natural sunlight. By tracing its evaporation performance every day and cycling use, neither structural degradation nor vapour generation rate decay was noticed (**Figure 3c** and **Figure S13, Supporting Information**), confirming the excellent mechanical and structural stability of the evaporator for long-term solar evaporation-based desalination in brine.

2.5 Electric output performance of the evaporator

Since the GMS@HCDs are rich in functional groups and porous structure, and have good electrical conductivity, it is possible to be applied as water evaporation-induced electricity generator. To realize this, two small pieces (0.5×0.5 cm) of graphite electrodes were stuck on the bottom and top surfaces of GMS@HCDs, respectively (**Figure 4a**). On account of the effect of the GMS@HCDs thickness on proton dissociation and diffusion, we first tested the GMS@HCDs with different thicknesses and identified the optimum value of 7.5 mm (**Figure S14, Supporting Information**). For simultaneous solar evaporation and electricity generation, a regulated GMS@HCDs evaporation (20 mm×20 mm×7.5 mm) was floated on the surface of real seawater collected from Bohai Sea. As expected, the GMS@HCDs can continuously generate a voltage of 0.86 V and a current of about 407.20 μA (101.80 $\mu A \cdot cm^{-2}$) along with a high water evaporation of 3.49 $kg \cdot m^{-2} \cdot h^{-1}$ under one sun irradiation (**Figure 4b**). The effective output power can reach 94.28 $\mu W \cdot cm^{-2}$ when the load resistance is 5.80 kΩ (**Figure 4c**) in 17.5 wt% NaCl solution under one sun, which is a very high value among the evaporation-enabled power generation devices reported to date [15, 21, 24-

26, 44-55] (**Figure 4d** and **Table S2, Supporting Information**). Therefore, this evaporator is capable of producing simultaneously great amount of clean water and electricity using solar light and seawater.

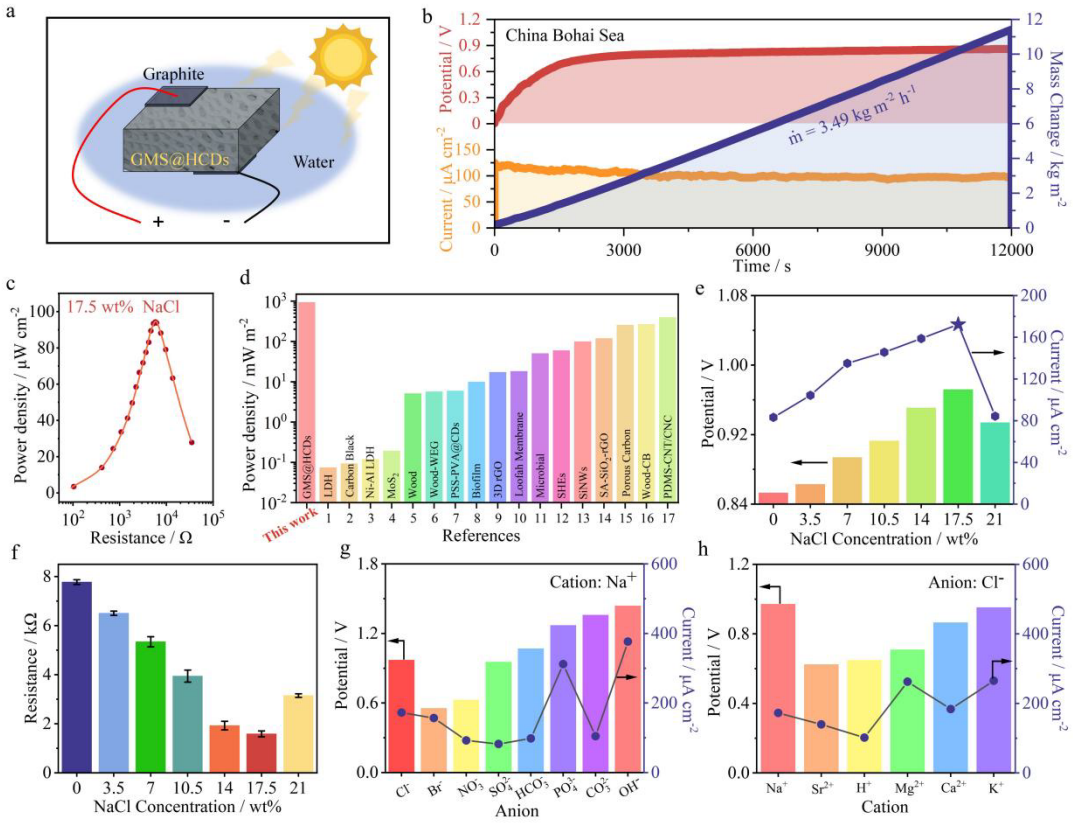


Figure 4. Electric output performance of the evaporator. **a**) Schematic illustration of electricity collection; **b**) The voltage and current output along with water evaporation change of GMS@HCDs as a function of time in real seawater; **c**) Power density output of GMS@HCDs in 17.5 wt% NaCl solution with variable electric resistance; **d**) Comparison of power output from GMS@HCDs with known generators; **e**) The effect of the brine salinity on the voltage and current output of GMS@HCDs; **f**) The dependence of the GMS@HCDs resistance on the brine salinity; **g**) The effect of the anions on the voltage and current output of GMS@HCDs; **h**) The effect of the cations on the voltage and current output of GMS@HCDs.

The effects of the cations and anions and their concentrations on electricity generation capacity of GMS@HCDs were investigated systematically. **Figure 4e** showed the dependence of open-circuit voltage and the short-circuit current density on the concentration of NaCl. The induced voltage and current density exhibited initial ascending then descending variation along with increasing NaCl concentration. The GMS@HCDs in 17.5 wt% NaCl solution delivered the highest voltage output (0.972 V) and current density (172.38 μA•cm^{-2}). The

current density of GMS@HCDs in 21 wt% NaCl solution remarkably decreased. To uncover the reason, the resistances of GMS@HCDs in NaCl solution with different concentrations were measured. As shown in **Figure 4f**, the resistance rose abnormally at the concentration of 21 wt% NaCl, which was also verified by EIS spectra (**Figure S15, Supporting Information**). This increased resistance gave rise to the decreased current density in 21 wt% NaCl solution. More interestingly, the power generation of GMS@HCDs varied with the kinds of cation and anion present in solution as well. With the same concentration of Na^+ ion, it was found that the anions of OH^-, CO_2^{2-}, PO_4^{3-} could significantly boost the electric output of GMS@HCDs (**Figure 4g**). For example, the GMS@HCDs in 17.5 wt% NaOH solution generated a maximum voltage of 1.44 V and a maximum current density of 376.41 μA•cm^{-2}. In contrast, most cations cannot improve the power generation of the evaporator when Cl^- ion served as the anion in solution (**Figure 4h**).

2.6 The continuous electricity-generating mechanism

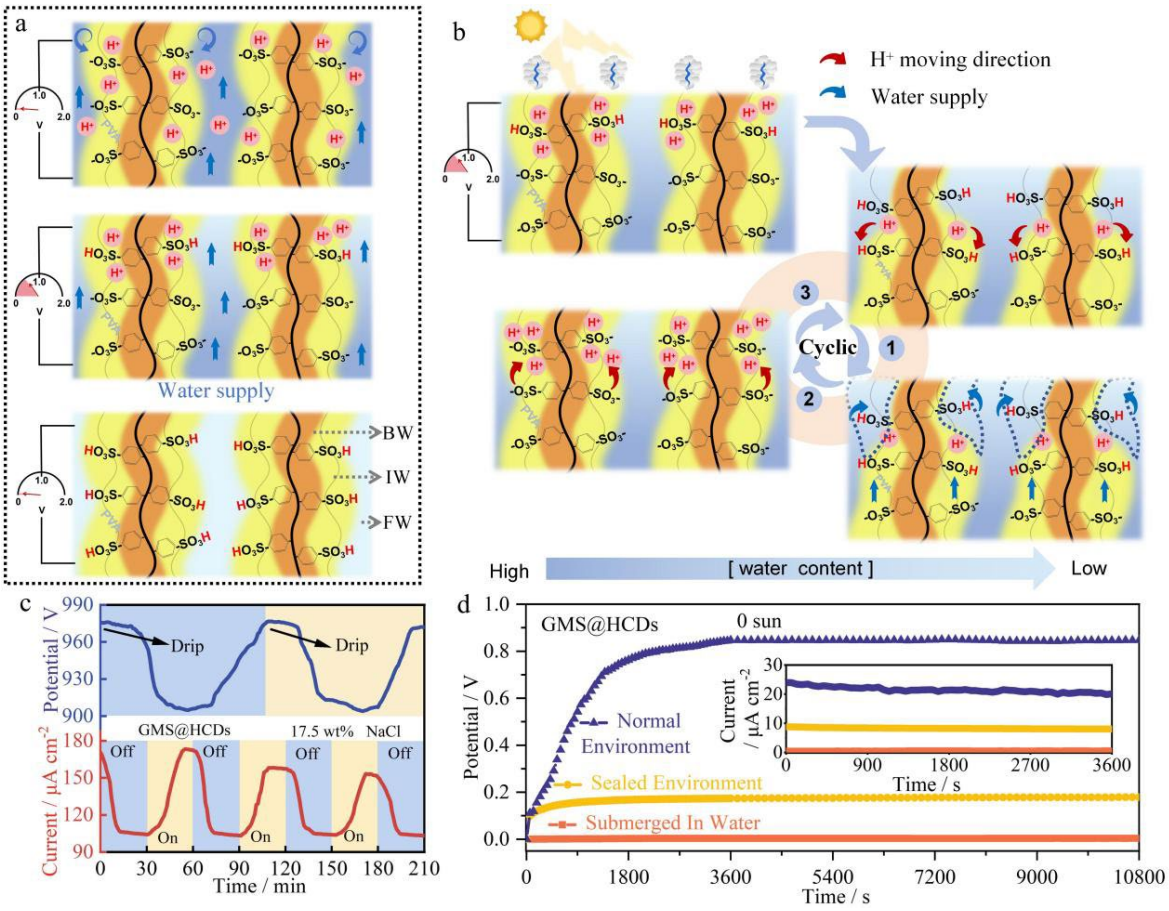


Figure 5. The continuous electricity-generation mechanism. **a**) Schematic illustration of water-enabled electricity generation in a GMS@HCDs without water evaporation; **b**) Schematic illustration of evaporation-driven continuously electric generation in a GMS@HCDs; **c**) The voltage responses to a brine droplet dripped on the surface of

GMS@HCDs (Top) and the current responses of GMS@HCDs to light source switch; **d**) Electric output performances of GMS@HCDs in different conditions (without illumination, sealed the surface and submerged in water).

As a polyelectrolyte, PSS contains abundant sulfonated groups that can release mobile protons in water (**Figure 5a, bottom** and **Figure S6, Supporting Information**). With water feed into PSS, the protons will be dissociated from PSS and then diffuse along the water flow direction driven by the proton concentration difference, leading to an internal electric field and an output current (**Figure 5a, middle**). After water saturation in PSS, it is difficult to confine protons in local IW region, where water molecules are endowed with a weaker hydrogen bond than that of bound water (BW) and more liable to bond with the protons to form H_3O^+ ions. When the protons diffuse from IW to FW region, the mobility of protons is completely released and causes their back diffusion under electrostatic interaction (**Figure 5a, top**). Finally, the proton concentration gradient is eliminated, making the electric output gradually decreases back to zero. Distinguished from these mechanisms and phenomena reported previously [24, 26], the electric signals of our evaporator did not disappear but sustained throughout the solar evaporation processes over the GMS@HCDs. This implied that the homogeneity of water molecules within the GMS@HCDs cannot be reached during the evaporation process according to the reported power generation mechanism. During interfacial solar evaporation, the IW with the lowest vaporization enthalpy is evaporated preferentially on the top surface of GMS@HCDs (**Figure 5b**,). Therefore, the mobile protons are forced to move back to the bottom and reverse dissociation reaction occurs due to the reduction in IW (Step 1). As a result, the FW fills the space left by the evaporated IW (Step 2). Thus, the dissociation and diffusion of the protons replay and then induce current and voltage again (Step 3). Actually, this circular process is instantaneous and iterative during solar water evaporation, thereby the electricity generation from GMS@HCDs can be sustained. To examine the proposed persistent electricity-generating mechanism, a drop of water was placed on the surface of GMS@HCDs during solar water evaporation. As expected, a visible reduction in the output voltage followed by a gradual increase to the original level along with solar evaporation was observed, indicating the presence of evaporation-driven proton concentration difference (**Figure 5c, top**). Moreover, the output current from GMS@HCDs significantly fluctuated with off-on light source, reflecting the contribution of solar irradiation/evaporation on power generation (**Figure 5c, bottom**). To further illustrate the mechanism, the GMS@HCDs was submerged in pure water, where the proton concentration gradient cannot be formed in the GMS@HCDs due to the water saturation. As expected, no

voltage output was detected **(Figure 5d**). In another case, the top evaporation surface of GMS@HCDs was sealed to impede water evaporation. As a result, the voltage dramatically dropped from 0.86 to <0.2 V, confirming that water evaporation promoted the continuous power generation of GMS@HCDs **(Figure 5d**).

Molecular dynamics (MD) simulations were conducted to investigate the dissociation reaction of sulfonated groups in the PSS-H_2O system (**Figure S16** and **S17, Supporting Information**). A snapshot of the PSS-H_2O system with a small amount of H_2O molecules showed that H^+ ions were mainly bonded with -SO_3H (**Figure S17a, Supporting Information**). Radial distribution function (RDF) and coordination number (CN) were calculated to determine the coordination ability of H^+ with H_2O and -SO_3^- (**Figure S17b, Supporting Information**). The sharp peaks located at 1.8 and 2.1 Å were assigned to the SO_3-H^+ and H_2O-H^+, while the corresponding CNs were 0.73 and 2.03, respectively. When PSS-H_2O system contained a large amount of H_2O molecules, the snapshot displayed that H^+ ions were mainly combined with H_2O (**Figure S17c, Supporting Information**). The calculated CNs of the SO_3-H^+ and H_2O-H^+ were 0.57 and 2.82, respectively (**Figure S17d, Supporting Information**). MD simulated results indicated that the dissociation reaction of sulfonated groups depended on the content of water in the system. Thus, the number of free H^+ could be regulated with the number of changes of water molecules in the system, leading to persistent power output during solar water evaporation processes. In addition, the electrokinetic effect in GMS@HCDs during solar evaporation including proton transportation and potential distribution in the transient and steady state, were investigated using a finite element simulation based on Nernst-Planck equation and Poisson equations [56-57] (**Figure S18, Supporting Information**). Driven by solar evaporation, water flows from the bottom towards the top evaporation surface. The simulated results (**Figure S18a** and **Video S1, Supporting Information)** illustrated the changes in the proton concentration and potential distribution across GMS@HCDs during the evaporation processes. For proton concentration distribution, a large number of protons dissociated from PSS migrated with the water flow (i.e., advection), moved upward and accumulated at the top surface to form a concentration gradient of proton (**Figure S18a, Supporting Information**). Along with the change of proton concentration distribution, the potential difference between the bottom and top surfaces gradually increased and reached 0.82 V when the advection and diffusion of the protons reached the equilibrium state after 30 mins (**Figure S18b, Supporting Information**), which was consistent with experimental results. It is worth noting that the proton concentration distribution along the vertical direction does not increase linearly, which could be ascribed to different

concentration diffusion caused by the much higher evaporation rate on the top surface. The simulation results also further validate the proposed persistent electricity-generating mechanism of GMS@HCDs during evaporation processes.

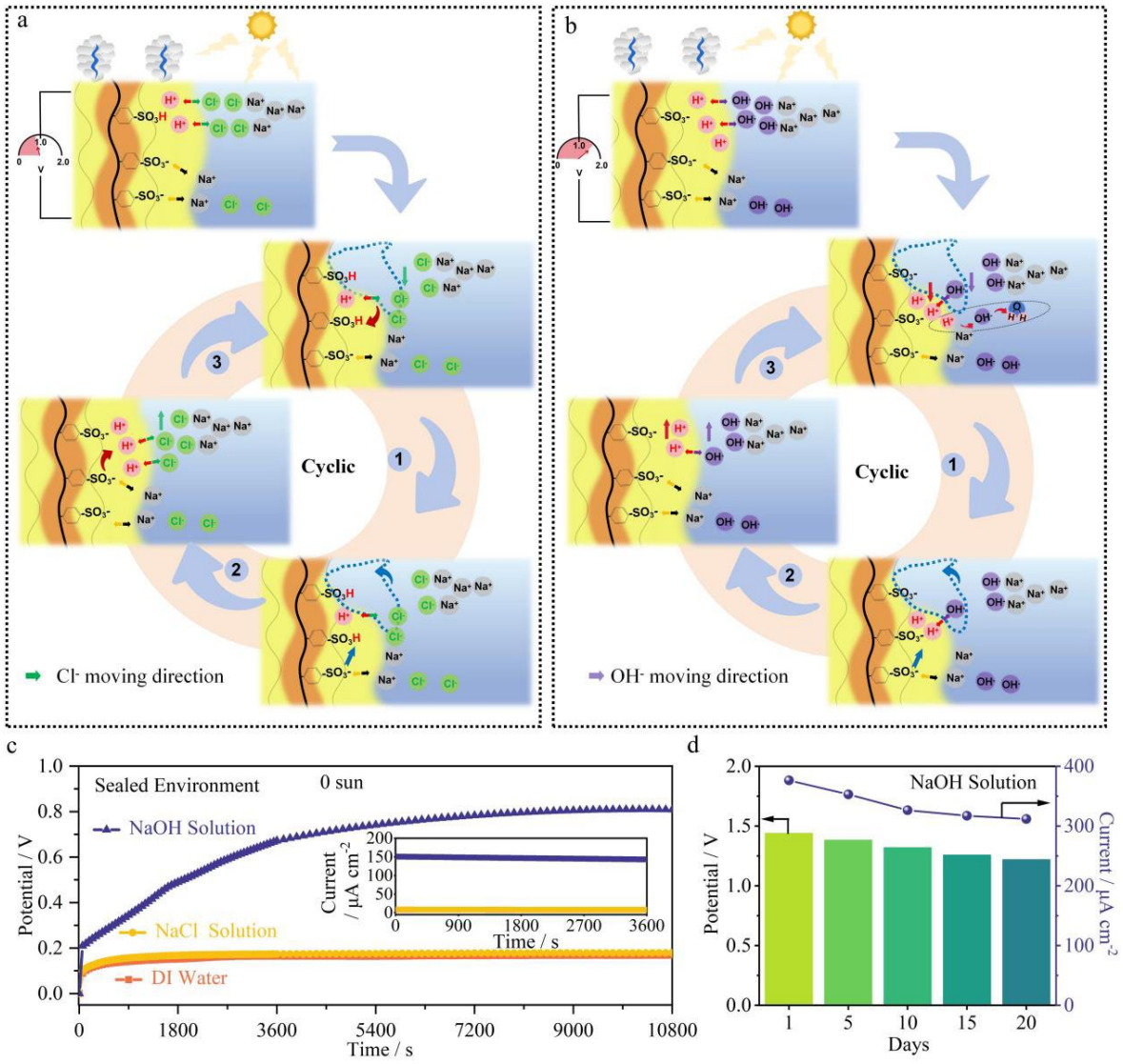


Figure 6. The influences of various ions on electricity-generation mechanisms. **a**) Schematic illustration for the influences of NaCl solution on continuously electric generation in a GMS@HCDs; **b**) Schematic illustration for the influences of NaOH solution on continuously electric generation in a GMS@HCDs; **c**) Electric output performances of surface-sealed GMS@HCDs in DI water, NaCl and NaOH solutions; **d**) The power generation test of GMS@HCDs in NaOH solution for 20 days.

Water can effectively solvate salts to ions. After solvation, the proton concentration field in GMS@HCDs will perturb the distribution of anions and cations in the hydration layer, leading to the formation of an electrical double (ED) layer near the region of FW and IW

(**Figure 6a**). Similar to continuous electricity generation mechanism, the IW vaporization breaks the balance of the original double charge layer and subsequently pushes ions in ED layer moving in the opposite direction to the proton concentration. Taking an example of NaCl solute, the Cl^- ions in ED layer migrate from top to bottom under the attraction of Na^+ ions (Step 1). After that, the FW accesses to IW region and enables more protons release once again (Step 2). Thus, the Cl^- ions tend to move back, but the IW rapidly evaporates again (Step 3). Then a new circulation starts. Synchronously, the outer Na^+ ions neighbouring Cl^- ion layer don't have time to adjust and then induce a local electric field in FW region that is just consistent with the direction of the proton concentration potential. Consequently, the solute-induced ion electric field can elevate the output electricity of GMS@HCDs. Compared with NaCl, alkaline solutes such as NaOH, Na_2CO_3 and Na_3PO_4, have an additional effect on ion-electric-field formation. This is because they can accelerate the dissociation reaction of sulfonated groups and/or even react with free protons, causing greater disequilibrium for anions and cations in ED layer (**Figure 6b** and **Figure S19, Supporting Information**). Thus, the ion electric field could be enhanced significantly and thereupon pulls up the whole power output amount of GMS@HCDs. To verify this proposition, we sealed the surface of GMS@HCDs in different solute solutions to limit water evaporation and measured the corresponding voltage output. Lack of dynamic cyclic process induced by solar water evaporation, the generated voltage of GMS@HCDs in 17.5 wt% NaCl solution becomes the same as that in pure water (**Figure 6c**), proving absence of static ion electric field in evaporator. However, the voltage of GMS@HCDs in NaOH solution remains at ~0.8 V generated under the same sealed environment, indicating the effect of anions on ED layer by interfering with the dissociation reaction of sulfonated groups (**Figure 6c**). Besides, after undergoing for 20 days, the power generation performance of GMS@HCDs in NaOH solution is still higher than that in NaCl solution and pure water (**Figure 6d**). This result certified that the proton concentration field and its induced ion electric field are still present in GMS@HCDs during solar evaporation.

2.7 Scalable integration of GMS@HCDs and application

The scalable integration of GMS@HCDs units is critical for control of high-performance power output during solar interfacial water evaporation. The voltage and current output of the integrated GMS@HCDs basically enhance linearly with the number of serial or parallel units (**Figure 7a**). This power output is sufficient for running lots of commercial electronic devices without the help of capacitors or rectifiers. **Figure 7b** shows an 8-digit electronic calculator that can do arithmetic operations when powered by four GMS@HCDs

units connected in series (**Video S2, Supporting Information**). Surprisingly, a high voltage of 56.6 V is readily produced by connecting 60 units in series under one sun (**Figure 7c**) and can light a dozen of red LED bulbs (1.8 V, 2 mA; **Figure 7d** and **Video S3, Supporting Information**). Most importantly, the stable power generation and evaporation rate were achieved during the 10 day continuous test in 17.5 wt% NaCl solution with 1 sun irradiance (**Figure 7e**), which is the best result ever reported for long-term power generation and solar desalination in highly concentrated saline water. The condensed water quality was estimated by the ohmic value achieved from a resistance measurement by a multimeter at a constant distance between electrodes (**Figure S20a, Supporting Information**). The resistance value of purified water is close to that of DI water (**Figure S20b, Supporting Information**), confirming effective purification of brine [28]. Moreover, GMS@HCDs is able to function well under strong acid conditions (**Figure 7f**). It should be pointed out that the acidic condition could suppress the dissociation of sulfonated groups, thus lowering the overall power generation of GMS@HCDs. As shown in **Figure 7g**, the voltage output of GMS@HCDs remained stable in a wide temperature range from 1 to 95 ℃, while the corresponding current output steadily increased with temperature rise due to acceleration of free proton motion. All of the above results verified the excellent stability and broad adaptability of GMS@HCDs.

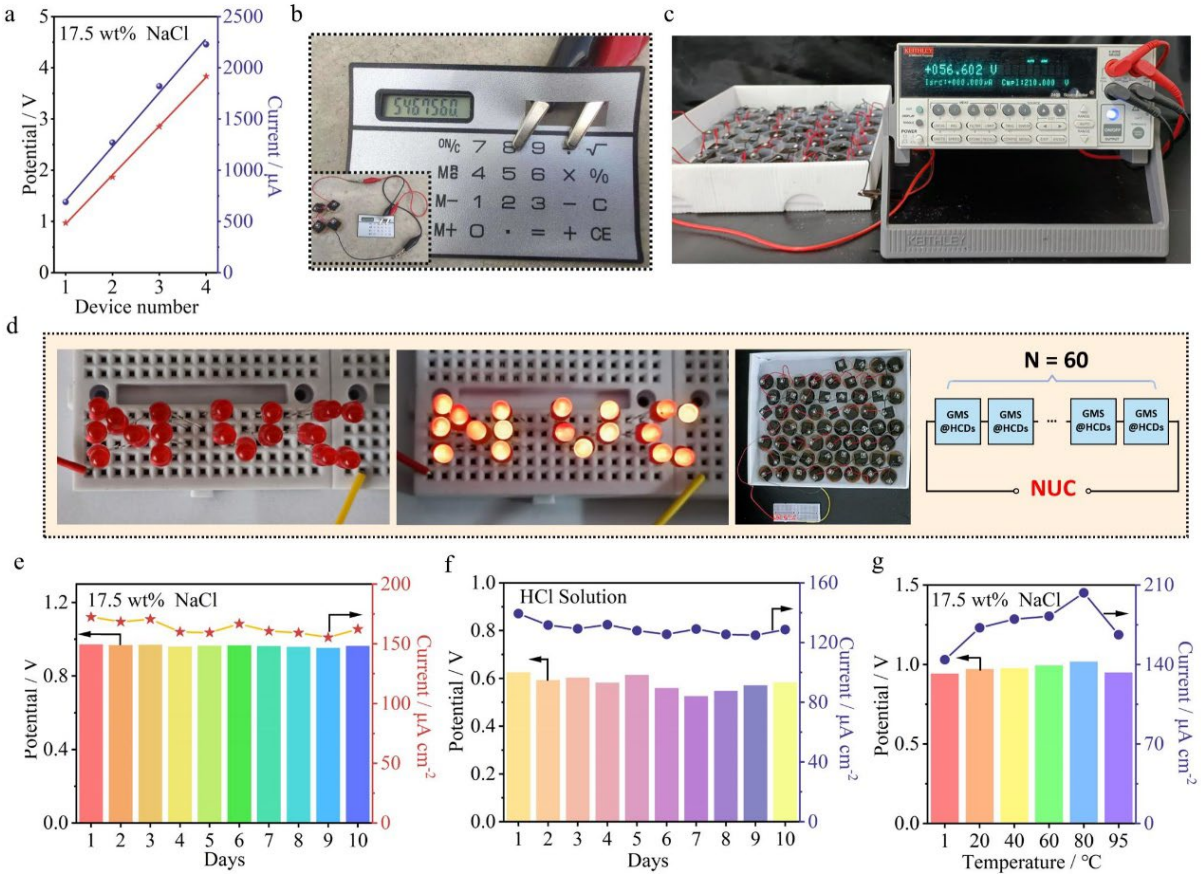


Figure 7. Integration and application of GMS@HCDs units. **a**) Electric outputs of GMS@HCDs units connected in series and in parallel; **b**) Four PMEG units connected in series capable of powering an electronic calculator for normal calculations; **c, d**) A high output voltage of 56.6 V generated by connecting 60 units in series under one sun (c) and a dozen of red LED bulbs were lighted (d); **e-g**) Stability and durability of electric generation performance of GMS@HCDs in 17.5 wt.% NaCl solution (e), 3.6 M HCl solution (f) and the temperature ranging from 1 to 95 ℃ (g).

3. Conclusion

We have presented a new type of bifunctional evaporator coupling with highly efficient salt-rejection and continuous electric generation by rational design of the polyelectrolyte hydrogel-functionalized photothermal sponge. This evaporator not only exhibits an unprecedentedly high water evaporation rate of 3.53 kg m^{-2} h^{-1} along with 98.6% solar energy conversion efficiency, but also can uninterruptedly deliver a voltage output of 0.972 V and a current density of 172.38 μA•cm^{-2} in high-concentration brine over a long period under one sun of irradiation. Furthermore, GMS@HCDs units can be scaled up by simple parallel or series connection to power a range of common electronic devices. Water evaporation from GMS@HCDs is the key for maintaining the proton concentration gradient and directional transport within the hydrogel of PSS and PVA. The control experiments reveal that the water-enabled proton concentration fields in IW region can induce an additional ion electric field in FW region based on solute solvation, thus leading to the enhanced electricity output amount. Given the low-cost materials, simple self-regeneration design, scalable fabrication process and stable performance, this work offers a promising strategy for addressing the shortage problem of freshwater resources and sustainable electricity.

4. Experimental Section

4.1 Sample preparation

First of all, MS blocks with a dimension of 20×20×7.5 mm were cleaned with both anhydrous ethanol and deionized water and then dried at 60 °C. Graphene oxides (GOs) were prepared from natural graphite powders using the modified Hummer method [58]. Colloidal GO suspensions of different concentrations (5, 10, 15 and 20 mg•mL^{-1}) were prepared by dilution with deionized water. After that, the porous MS was completely immersed in GO suspensions with different concentrations. After evaporating the solvent in the vacuum glow-ovens (60 ℃), the obtained GOs-wrapped MS was placed in HI solution (HI≥45.0 wt.%) at 95 ℃, and reacted for 40 s. Subsequently, the resultant samples were washed with anhydrous

ethanol and deionized water for 3 to 5 times to remove residual HI. After drying, the samples of GMS containing different masses of rGOs were obtained.

Coal-pitch-based CDs were obtained by selective oxidation etching of coal tar pitch with a mixture of hydrogen peroxide and formic acid following our previous report [59]. Under ultrasonic stirring, the different amounts of CDs were added in the same volume of PSS solution to acquire PSS-CDs solution containing various concentrations of CDs (i.e. 10, 20, 30, and 40 mg•mL^{-1}). Meanwhile, the different masses of PVA powders (0.5, 1, 1.5 and 2 g) and 125 μL of glutaraldehyde were added into 10 mL DI water to obtain homogeneous PVA-GA solution by heating at 90 ℃ for 2 h. Next, the GMS samples were firstly soaked into as-prepared PSS-CDs solution and then taken out to dry at 60 ℃ for 30 min. The acquired dry samples were immersed into PVA-GA solution to perform polymerization and cross-linking for 10 min. After washing with DI water, the samples were frozen at -10~-20 ℃ for 4 h to obtain GMS@HCDs

4.2 Sample characterization

The surface morphology and porous structure of the samples were observed on a scanning electron microscope (Tescan Mira LMS). Absorption spectra were collected on a UV-Vis-NIR spectrophotometer (Shimadzu UV3600) with an integrated sphere in the range of 250-2500 nm wavelengths. X-ray diffraction (XRD) patterns were recorded on the X-ray diffractometer (XRDynamic 500). The Raman spectra were recorded via a spectrometer (Thermo Fisher DXR 2xi). The excitation light for the Raman emission was generated by a YAG laser that had a single-mode operation at 532 nm. The evaporation enthalpies of the samples were measured by differential scanning calorimetry (DSC Q2000, TA Thermal Analysis Instruments). The electrochemical experiments were conducted with a electrochemical workstation (Bio-logic SP 200, France). A multimeter (VICTOR201, VICTOR Instrument) was used to test the resistance of the samples.

4.3 Solar water evaporation experiment

The samples with a dimension of 20 mm×20 mm×7.5 mm were placed into a homemade thermal-insulating foam floating on water in a cylinder container filled with enough water or brine. A small hole was drilled in the bottom of the foam to provide a channel for cotton threads to pump water. The setup was placed on an electronic balance for real-time recording of the mass change of the solution in the setup, and the resultant data were collected to calculate the evaporation rates according to the projection area. A solar simulator (CEL-HXUV300, CEAULIGHT, China) with an AM1.5 G optical filter was used as the light source, and the power density was measured by a power meter (China Education Au-light, CEL-

NP2000, China). The temperatures of evaporation surfaces were tested using a dual-channel thermometer (Xinster HT-9815).

4.4 Electric output measurement

The upper and bottom surfaces of the sample (20×20×7.5 mm) were connected with graphite electrodes. The solar simulator with AM1.5G filter was used as the light source. The device was connected to the electrochemical workstation (Bio-logic SP 200, France) for monitoring the signals of electric output. To avoid any inference from the static electricity, all the samples were short circuited before testing.

Supporting Information

Supporting Information is available from the Wiley Online Library or from the author.

Acknowledgements

This work is jointly supported by the special fund for Science and Technology Innovation Teams of Shanxi Province (202304051001014), Fundamental Research Program of Shanxi Province of China (20210302123037), Research Project Supported by Shanxi Scholarship Council of China (2022-136) and Australian Resaerch Council (DP220100583, FT190100485).

Conflict of Interest

The authors declare no conflict of interest.

Received: ((will be filled in by the editorial staff))

Revised: ((will be filled in by the editorial staff))

Published online: ((will be filled in by the editorial staff))

References

[1] M. Rodell, J. S. Famiglietti, D. N. Wiese, J. T. Reager, H. K. Beaudoing, F. W. Landerer, M. H. Lo, *Nature* **2018**, *557*, 651.

[2] B. R. Sutherland, *Joule* **2019**, *3*, 319.

[3] J. Gong, C. Li, M. R. Wasielewski, *Chem. Soc. Rev.* **2019**, *48*, 1862.

[4] L. Zhou, X. Li, G. W. Ni, S. Zhu, J. Zhu, *Natl. Sci. Rev.* **2019**, *6*, 562.

[5] L. Zhu, M. Gao, C. K. N. Peh, G. W. Ho, *Nano Energy* **2019**, *57*, 507.

[6] L. Zhang, X. Li, Y. Zhong, A. Leroy, Z. Xu, L. Zhao, E. N. Wang, *Nat. Commun.* **2022**, *13*, 849.

[7] X. Cui, Q. Ruan, X. Zhuo, X. Xia, J. Hu, R. Fu, Y. Li, J. Wang, H. Xu, *Chem. Rev.* **2023**, *123*, 6891.

[8] L. Li, J. Wang, C. Xue, Q. Chang, J. Yang, S. Hu, *Chem. Eng. J.* **2023**, *477*, 147185.

[9] F. Zhao, Y. Guo, X. Zhou, W. Shi, G. Yu, *Nat. Rev. Mater.* **2020**, *5*, 388.

[10] F. Zhao, X. Zhou, Y. Shi, X. Qian, M. Alexander, X. Zhao, S. Mendez, R. Yang, L. Qu, G. Yu, *Nat. Nanotechnol.* **2018**, *13*, 489.

[11] Y. Guo, J. Bae, Z. Fang, P. Li, F. Zhao, G. Yu, *Chem. Rev.* **2020**, *120*, 7642-7707.

[12] H. Zhang, N. He, B. Wang, B. Ding, B. Jiang, D. Tang, L. Li, *Adv. Mater.* **2023**, *35*, 2300398.

[13] N. He, H. Wang, F. Li, B. Jiang, D. Tang, L. Li, *Energy Environ. Sci.* **2023**, *16*, 2494.

[14] S. Yang, X. Tao, W. Chen, J. Mao, H. Luo, S. Lin, L. Zhang, J. Hao, *Adv. Mater.* **2022**, *34*, 2200693.

[15] T. G. Yun, J. Bae, A. Rothschild, I. D. Kim, *ACS Nano* **2019**, *13*, 12703.

[16] C. Du, X. Zhao, X. Qian, C. Huang, R. Yang, *Nano Energy* **2023**, *107*, 108086.

[17] J. Kim, E. J. Bae, Y. H. Kang, C. Lee, S. Y. Cho, *Nano Energy* **2020**, *74*, 104824.

[18] J. Zou, M. Zhang, J. Huang, J. Bian, Y. Jie, M. Willander, X. Cao, N. Wang, Z. L. Wang, *Adv. Energy Mater.* **2018**, *8*, 1702671.

[19] P. Yang, K. Liu, Q. Chen, J. Li, J. Duan, G. Xue, Z. Xu, W. Xie, J. Zhou, *Energy Environ. Sci.* **2017**, *10*, 1923-1927.

[20] L. Zhu, M. Gao, C. K. N. Peh, X. Wang, G. W. Ho, *Adv. Energy Mater.* **2018**, *8*, 1702149.

[21] B. Shao, Z. Song, X. Chen, Y. Wu, Y. Li, C. Song, F. Yang, T. Song, Y. Wang, S. T. Lee, B. Sun, *ACS Nano* **2021**, *15*, 7472.

[22] Y. Cheng, S. Cheng, B. Chen, J. Jiang, C. Tu, W. Li, Y. Yang, K. Huang, K. Wang, H. Yuan, J. Li, Y. Qi, Z. Liu, *J. Am. Chem. Soc.* **2022**, *144*, 15562-15568.

[23] C. Rosso, G. Filippini, M. Prato, *ACS Catal.* **2020**, *10*, 8090-8105.

[24] H. Wang, Y. Sun, T. He, Y. Huang, H. Cheng, C. Li, D. Xie, P. Yang, Y. Zhang, L. Qu, *Nat. Nanotechnol.* **2021**, *16*, 811.

[25] H. Wang, T. He, X. Hao, Y. Huang, H. Yao, F. Liu, H. Cheng, L. Qu, *Nat. Commun.* **2022**, *13*, 2524.

[26] Z. Yan, N. Li, Q. Chang, C. Xue, J. Yang, S. Hu, *Chem. Eng. J.* **2023**, *467*, 143443.

[27] J. Bai, Y. Huang, H. Wang, T. Guang, Q. Liao, H. Cheng, S. Deng, Q. Li, Z. Shuai, L. Qu, *Adv. Mater.* **2022**, *34*, 2103897.

[28] H. Zhou, C. Xue, Q. Chang, J. Yang, S. Hu, *Chem. Eng. J.* **2021**, *421*, 129822.

[29] C. Liu, Y. Peng, X. Zhao, *Desalination* **2021**, *501*, 114911.

[30] L. Noureen, Z. Xie, M. Hussain, M. Li, Q. Lyu, K. Wang, L. Zhang, J. Zhu, *Sol. Energy Mater. Sol. Cells* **2021**, *222*, 110952.

[31] X. Wang, L. Zhang, D. Zheng, X. Xu, B. Bai, M. Du, *Chem. Eng. J.* **2023**, *462*, 142265.

[32] W. Ren, H. Wang, Q. Chang, N. Li, J. Yang, S. Hu, *Carbon* **2021**, *184*, 102.

[33] B. Peng, Q. Lyu, M. Li, S. Du, J. Zhu, L. Zhang, *Adv. Funct. Mater.* **2023**, *33*, 2214045.

[34] W. Lei, Y. Liu, S. Khan, N. Suzuki, C. Terashima, A. Fujishima, M. Liu, *Desalination* **2022**, *533*, 115780.

[35] X. Xu, Q. Chang, C. Xue, N. Li, H. Wang, J. Yang, S. Hu, *J. Mater. Chem. A* **2022**, *10*, 11712.

[36] A. Chu, M. Yang, H. Yang, X. Shi, J. Chen, J. Fang, Z. Wang, H. Li, *ACS Appl. Mater. Interfaces* **2022**, *14*, 36116.

[37] Y. Wang, Q. Chang, C. Xue, J. Yang, S. Hu, *J. Colloid Interface Sci.* **2022**, *621*, 33.

[38] C. Xue, Y. Shen, Q. Zhang, Q. Chang, N. Li, Y. Li, W. Zheng, S. Hu, J. Yang, *Nano Res.* **2022**, *16*, 5953.

[39] Z. Wang, X. Wu, J. Dong, X. Yang, F. He, S. Peng, Y. Li, *Chem. Eng. J.* **2022**, *427*, 130905.

[40] J. Xu, G. Wang, L. Zhu, G. Jiang, Y. Lei, Z. Zeng, L. Xue, *Chem. Eng. J.* **2023**, *455*, 140704.

[41] B. Song, N. Li, Q. Chang, C. Xue, J. Yang, S. Hu, *ACS Appl. Mater. Interfaces* **2023**, *15*, 22123.

[42] X. Zhou, F. Zhao, Y. Guo, Y. Zhang, G. Yu, *Energy Environ. Sci.* **2018**, *11*, 1985-1992.

[43] N. He, Y. Yang, H. Wang, F. Li, B. Jiang, D. Tang, L. Li, *Adv. Mater.* **2023**, *35*, 2300189.

[44] J. Tian, Y. Zang, J. Sun, J. Qu, F. Gao, G. Liang, *Nano Energy* **2020**, *70*, 104502.

[45] J. Sun, P. Li, J. Qu, X. Lu, Y. Xie, F. Gao, Y. Li, M. Gang, Q. Feng, H. Liang, X. Xia, C. Li, S. Xu, J. Bian, *Nano Energy* **2019**, *57*, 269.

[46] D. He, Y. Yang, Y. Zhou, J. Wan, H. Wang, X. Fan, Q. Li, H. Huang, *Nano Energy* **2021**, *81*, 105630.

[47] Q. Y. Wu, C. Wang, R. Wang, C. Chen, J. Gao, J. Dai, D. Liu, Z. Lin, L. Hu, *Adv. Energy Mater.* **2019**, *10*, 1902590.

[48] T. Cai, L. Lan, B. Peng, C. Zhang, S. Dai, C. Zhang, J. Ping, Y. Ying, *Nano Lett.* **2022**, *22*, 6476.

[49] X. Liu, T. Ueki, H. Gao, T. L. Woodard, K. P. Nevin, T. Fu, S. Fu, L. Sun, D. R. Lovley, J. Yao, *Nat. Commun.* **2022**, *13*, 4369.

[50] G. Zhang, Z. Duan, X. Qi, Y. Xu, L. Li, W. Ma, H. Zhang, C. Liu, W. Yao, *Carbon* **2019**, *148*, 8.

[51] P. Luan, Y. Zhao, Q. Li, D. Cao, Y. Wang, X. Sun, C. Liu, H. Zhu, *Small* **2022**, *18*, 2104320.

[52] G. Ren, Q. Hu, J. Ye, X. Liu, S. Zhou, Z. He, *Chem. Eng. J.* **2022**, *441*, 135921.

[53] K. Liu, T. Ding, J. Li, Q. Chen, G. Xue, P. Yang, M. Xu, Z. L. Wang, J. Zhou, *Adv. Energy Mater.* **2018**, *8*, 1702481.

[54] T. Chen, D. Zhang, X. Tian, S. Qiang, C. Sun, L. Dai, M. Zhang, Y. Ni, X. Jiang, *Carbohydr. Polym.* **2022**, *294*, 119809.

[55] L. Zhu, T. Ding, M. Gao, C. K. N. Peh, G. W. Ho, *Adv. Energy Mater.* **2019**, *9*, 1900250.

[56] X.-S. Wang, D. He, J. J. Wylie, H. Huang, *Phys. Rev. E* **2014**, *89*, 022722.

[57] P. B. Warren, *Phys. Rev. Lett.* **2020**, *124*, 248004.

[58] J. Su, Q. Chang, C. Xue, J. Yang, S. Hu, *Carbon* **2022**, *194*, 267-273.

[59] X. Meng, Q. Chang, C. Xue, J. Yang, S. Hu, *Chem. Commun.* **2017**, *53*, 3074.

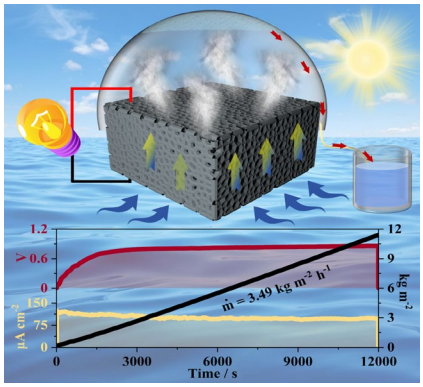
The table of contents entry:

A bifunctional solar evaporator is developed by designing polyelectrolyte hydrogel-functionalized photothermal sponge. This evaporator not only exhibits a water evaporation rate of 3.53 kg•m^{-2}•h^{-1}along with 98.6% solar energy conversion efficiency, but also can uninterruptedly deliver a voltage output of 0.972 V and a current density of 172.38 μA•cm^{-2} in brine over a prolonged period under one sun.

Lin Li, Chaorui Xue, Qing Chang, Jinlong Yang, Shengliang Hu* and Haolan Xu*

Polyelectrolyte Hydrogel-Functionalized Photothermal Sponge Enables Simultaneously Continuous Solar Desalination and Electricity Generation without Salt Accumulation

ToC figure



Supporting Information

Polyelectrolyte Hydrogel-Functionalized Photothermal Sponge Enables Simultaneously Continuous Solar Desalination and Electricity Generation without Salt Accumulation

Lin Li, Chaorui Xue, Qing Chang, Jinlong Yang, Shengliang Hu and Haolan Xu**

1. Materials and Chemicals

Commercial porous melamine sponge (MS) was purchased from Ledian Furniture Company of China without further treatment. Chemical reagents including HI, formic acid (88 v/v%), concentrated sulfuric acid (98 wt%), concentrated phosphoric acid (85 wt%), glutaraldehyde (GA, 50 wt% in the water) and anhydrous ethanol (AEA) were purchased from Damao Chemical Reagent Factory, China. Graphite powders, hydrogen peroxide (H_2O_2, 30 v/v%), polyvinyl alcohol (PVA, Mw ~75,000) and polystyrene sulfonic acid (PSS, Mw ~70,000) were purchased from Shanghai Aladdin Biochemical Technology Co., Ltd., China. All chemical reagents were directly used without further purification.

2. Supporting Results

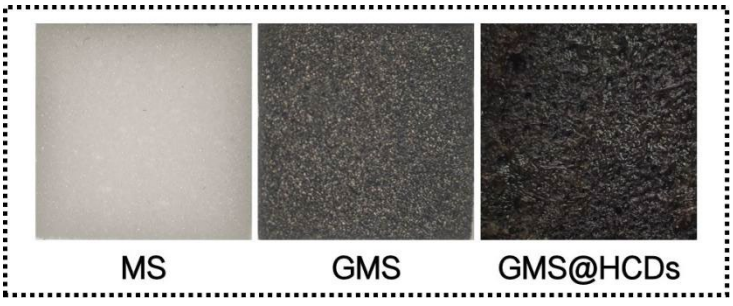


Figure S1. Photographs of MS, GMS and GMS@HCDs

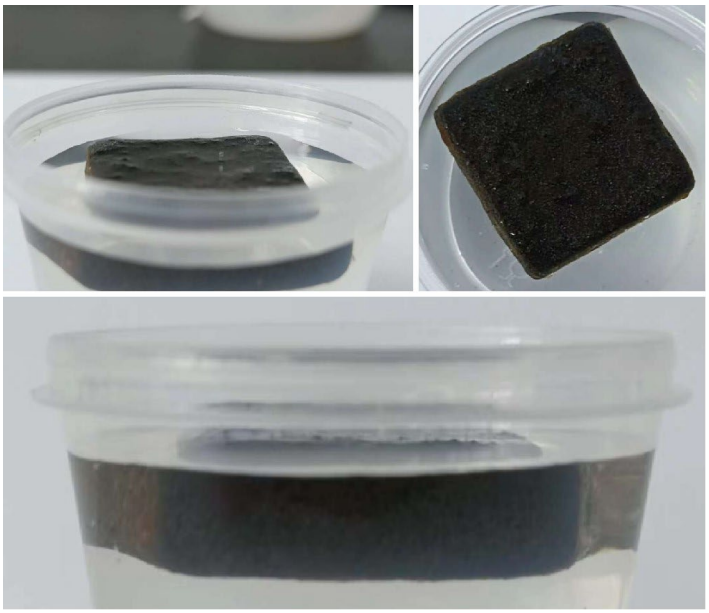


Figure S2. Photographs of GMS@HCDs floating on the water

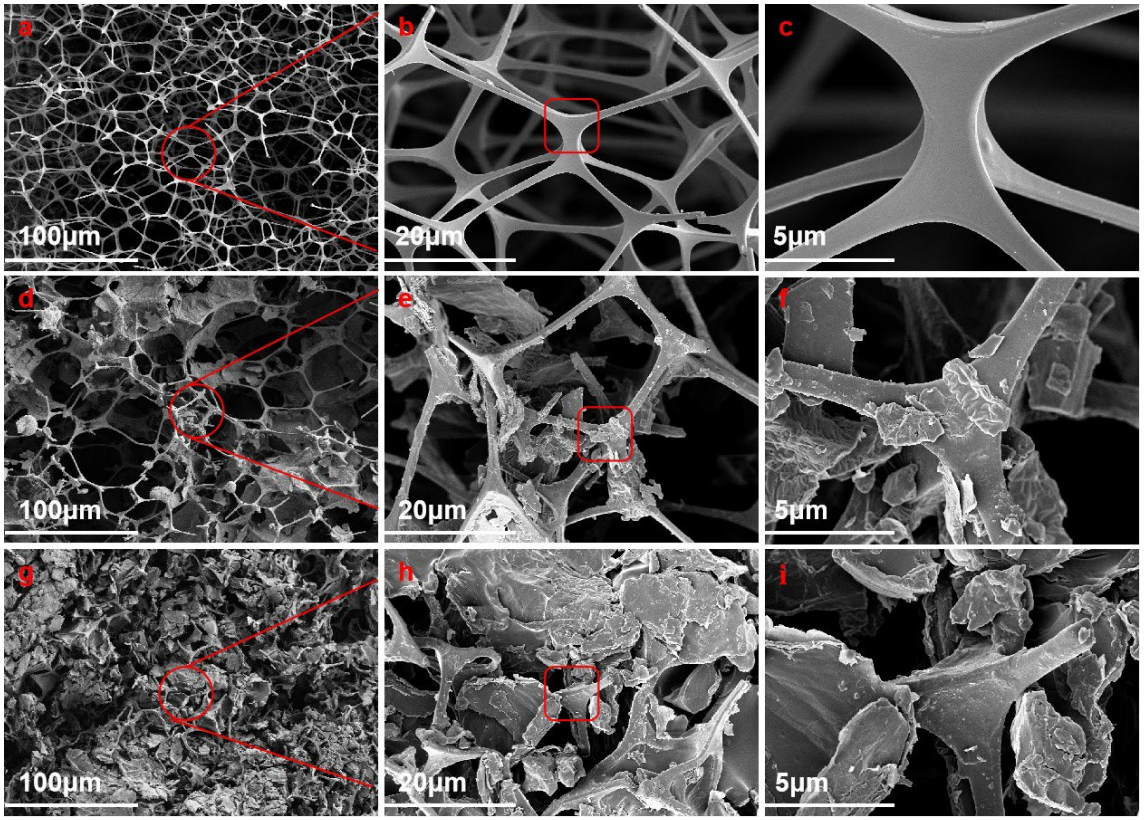


Figure S3. SEM images: (a-c) MS; (d-f) GMS; (g-i) GMS@HCDs

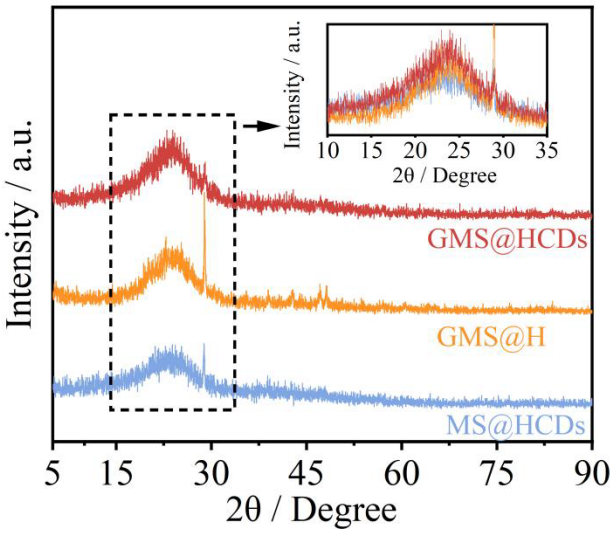


Figure S4. XRD patterns of MS@HCDs, GMS@H and GMS@HCDs

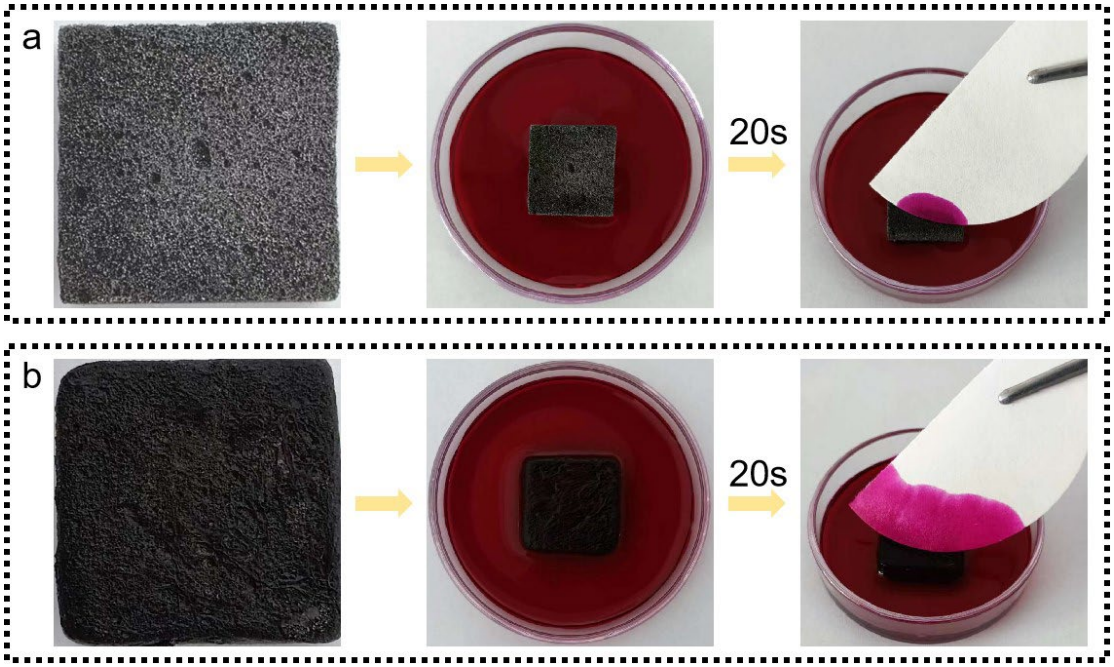


Figure S5. Comparison of water adsorption of GMS (a) and GMS@HCDs (b)

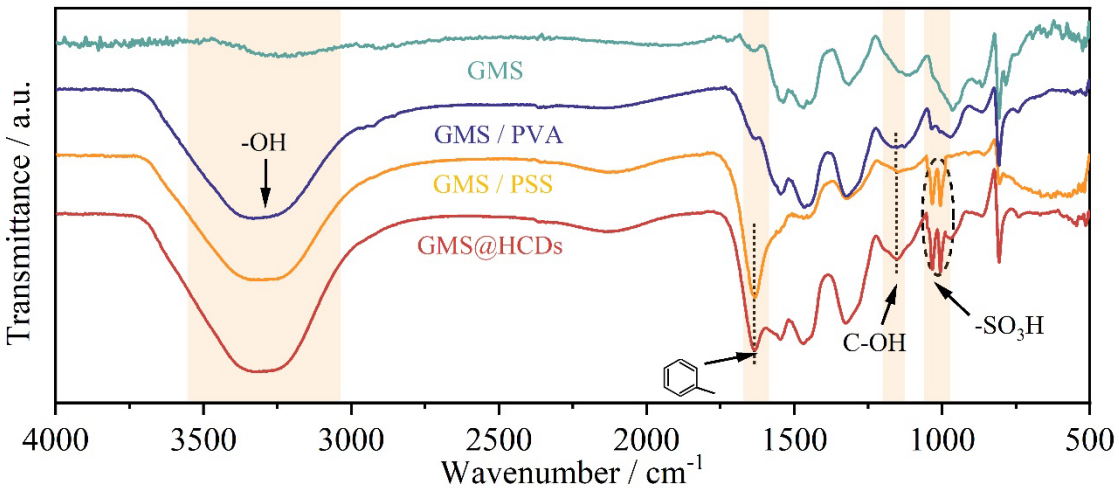


Figure S6. FTIR spectra of GMS, GMS/PVA, GMS/PSS and GMS@HCDs

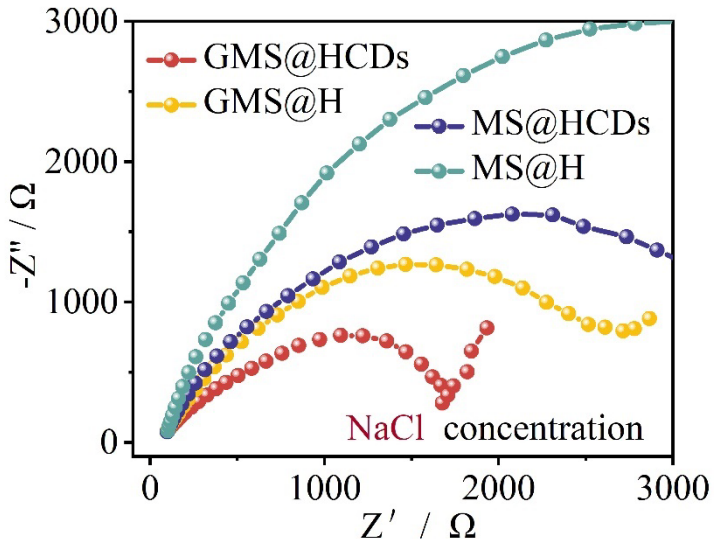


Figure S7. EIS plots of GMS@HCDs, GMS@H, MS@HCDs and MS@H in NaCl solution

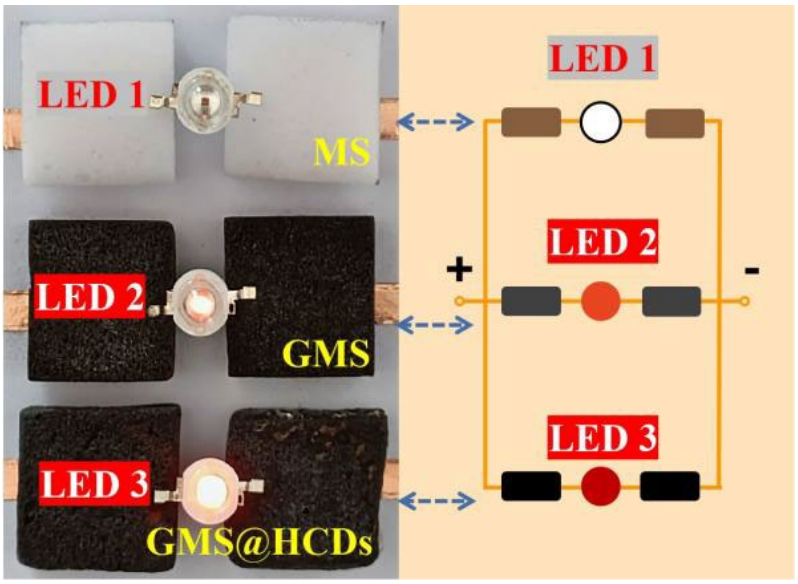


Figure S8. The photographs for two monoliths of GMS@HCDs showing more superior electric conductivity properties than GMS and MS by applying the same voltage

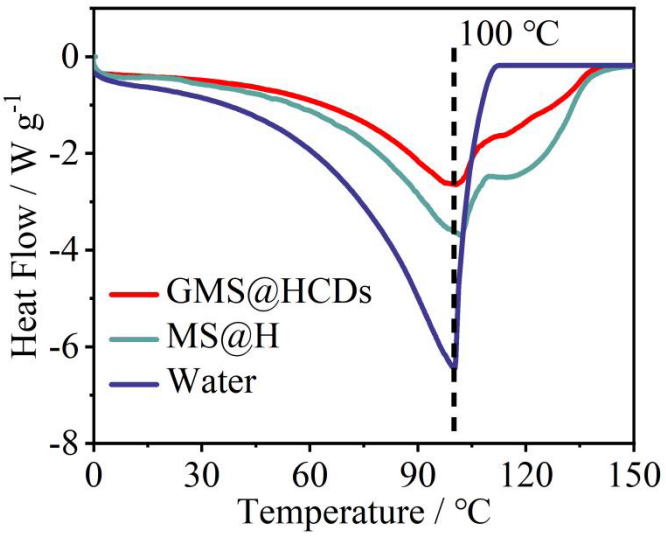


Figure S9. DSC curves of pure water, MS@H and GMS@HCDs

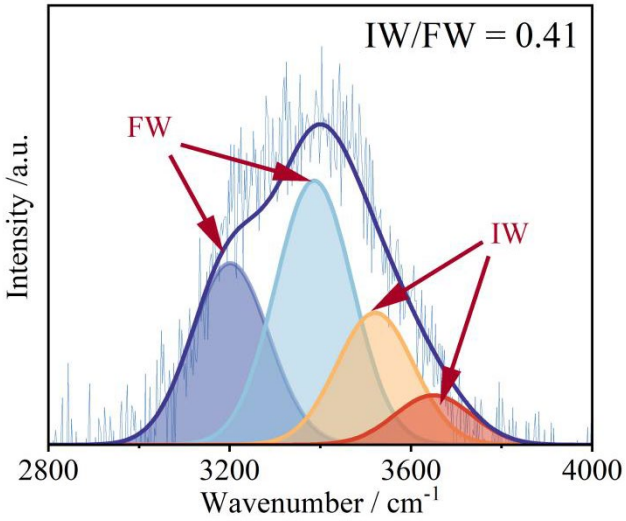


Figure S10. Raman spectra displaying the fitting peaks representing IW and FW in the GMS

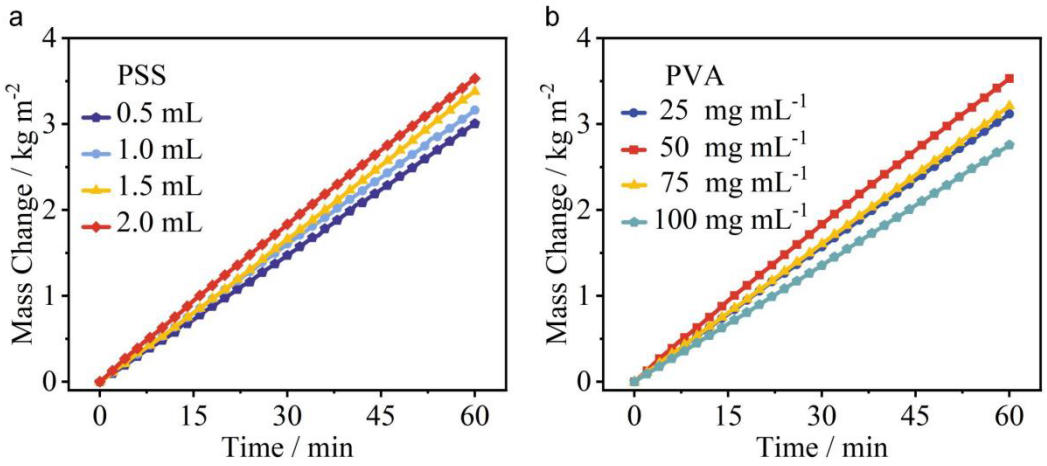


Figure S11. The effects of the amount of PSS (a) and PVA (b) on the evaporation performance of GMS@HCDs



Figure S12. Evaporation of anti-salt-fouling of GMS@HCDs with the presence of salt crystalline (100 mg NaCl) initially under natural sunlight

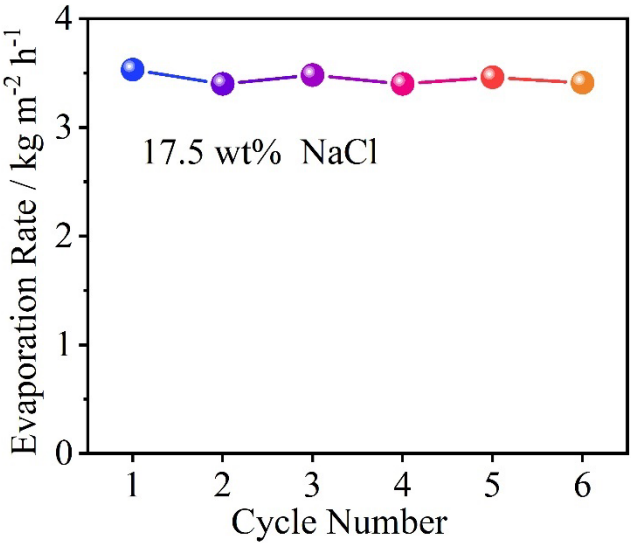


Figure S13. The cycling stability of GMS@HCDs in 17.5 wt.% NaCl brine

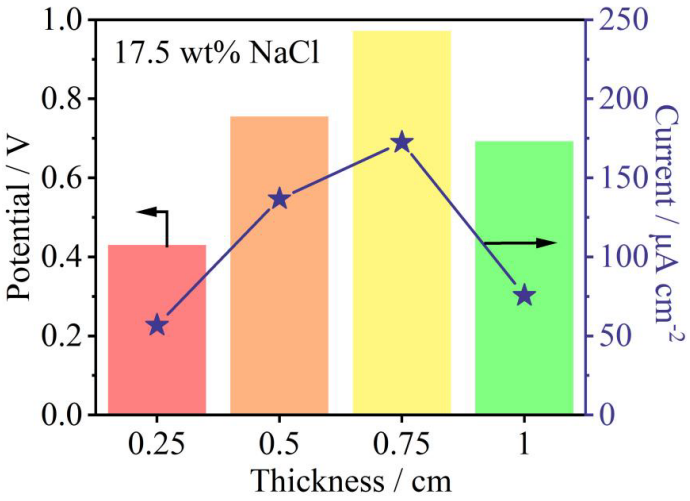


Figure S14. The effects of the thicknesses of GMS@HCDs on its electric output

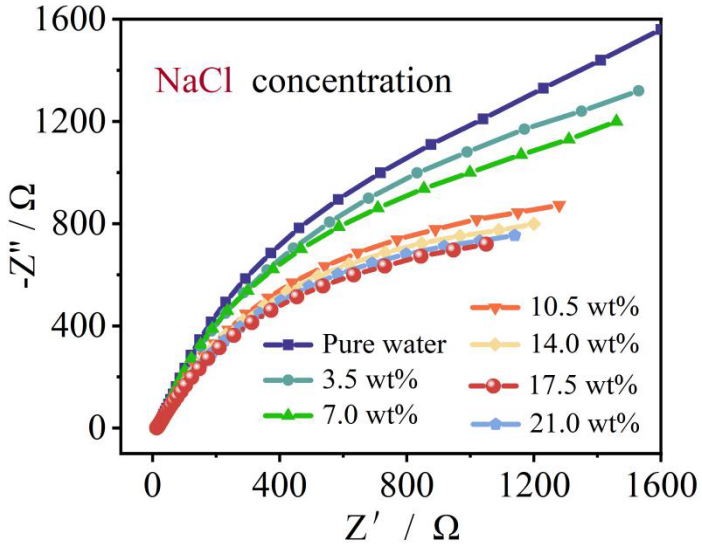


Figure S15. EIS plots of GMS@HCDs in different concentrations of NaCl solution

Molecular dynamic (MD) simulations were applied to investigate the coordination condition of H^+ in two considered PSS-H_2O solution systems, denoted as S1 and S2. The difference between S1 and S2 is the number of water molecules in simulations. For S1, the box contained 10 PSS monomers and 317 H_2O molecules, and for S2, the box was composed of 10 PSS monomers and 1325 H_2O molecules. All components were constructed into cubic simulation boxes. All MD simulations were carried out by using COMPASS force field [1-2]. Van der Waals and Coulomb interactions were respectively considered by atom based and Ewald methods with a cut-off value of 12.5 Å. Equations of motion were integrated with a time step of 1 fs. After energy minimization, each system was fully relaxed under periodic boundary conditions for 400 ps in the NPT (P = 1 atmosphere, T = 298 K) ensemble using the Nose thermostat and Berendsen barostat. After reaching the equilibrium state, another 400 ps simulation under NVT ensemble was performed to extract trajectory and data for radial distribution function (RDF) and coordination number (CN) calculation. The dynamic trajectory for each system was outputted at an interval of 4 ps. The coordination number N of H^+ in the first solvation shell was calculated as [3]:

$$N = 4\pi\rho\int_0^{R_M} g\,(r)r^2dr \qquad \text{(S1)}$$

in which R_M is the distance of the first minimum following the first peak in the RDF $g(r)$ and ρ is the number density of H^+.

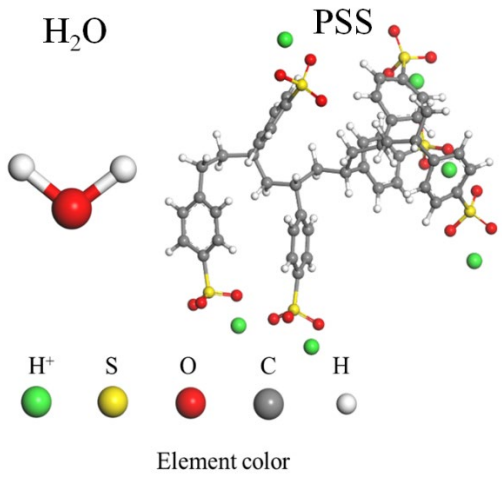


Figure S16. Atomic configurations of H_2O and PSS.

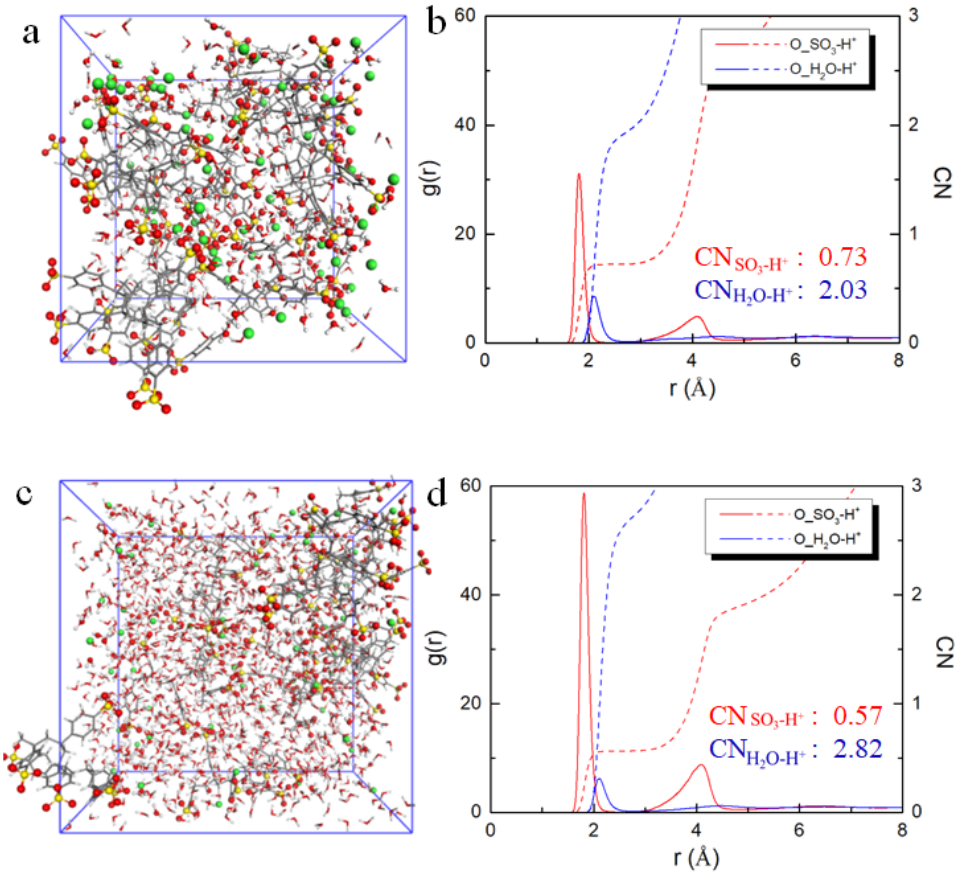


Figure S17. Molecular dynamic (MD) simulations. **a**, Snapshot of the MD simulation systems with a small amount of H_2O molecules (denoted as S1); **b**, The radial distribution function and coordination number (CN) for S1; **c**, Snapshot of the MD simulation systems with a large amount of H_2O molecules (denoted as S2); **d**, The radial distribution function and coordination number for S2.

To study the electrokinetic phenomenon of GMS@HCDs for electricity generation during solar evaporation, a three-dimensional geometric model corresponding to the actual GMS@HCDs sizes was built for finite element simulation by coupling Nernst-Planck equation and Poisson equations. For the Nernst-Planck equation, J_i is the flux vector of the ion concentration determined by the convective flux, concentration diffusion, and electromigration flux [4]

$$J_i = n_i u - D_i \nabla n_i - \frac{z_i e n_i D_i}{k_b \mathrm{T}} \nabla \varphi \quad \text{(S2)}$$

where n_i is the proton concentration, u is the fluid velocity, D_i is the diffusion coefficient, z_i is the valence, e is the elementary charge, k_b is the Boltzmann constant, T is the temperature, and φ is the double electric layer potential. Based on the Gauss electrostatic theorem, the Poisson equation is given [5]

$$\nabla(\varepsilon_r \varepsilon_0 \nabla \varphi) = -\rho_e u = -F \sum_{i=1}^{N} z_i n_i \quad \text{(S3)}$$

where ε_r is the dielectric constant of the water, ε_0 is the permittivity of vacuum, ρ_e is the density of electrostatic charge, and F is the Faraday constant.

The two Equations can be numerically solved with the aid of COMSOL software so as to determine the proton concentration and potential distribution. In the numerical simulation, the surface charge densities of GMS@HCDs were $-3e^{-5}$ C/m^2. To facilitate simulations, GMS@HCDs was idealized as a rectangular solid with a size of 20 × 20 × 7.5 cm. It is assumed that our system can be quantitatively explained by the equations with appropriate boundary conditions. The simulated temperature is 298 K, and the dielectric constant of the water is 78. The bottom is ground. The diffusion coefficient of proton is $1e^{-7}$ m^2/s. The proton flux and potential at boundaries satisfies the condition,

$$\vec{n} \cdot J_i = 0 \text{ and } \vec{n} \cdot \vec{D} = 0 \quad \text{(S4)}$$

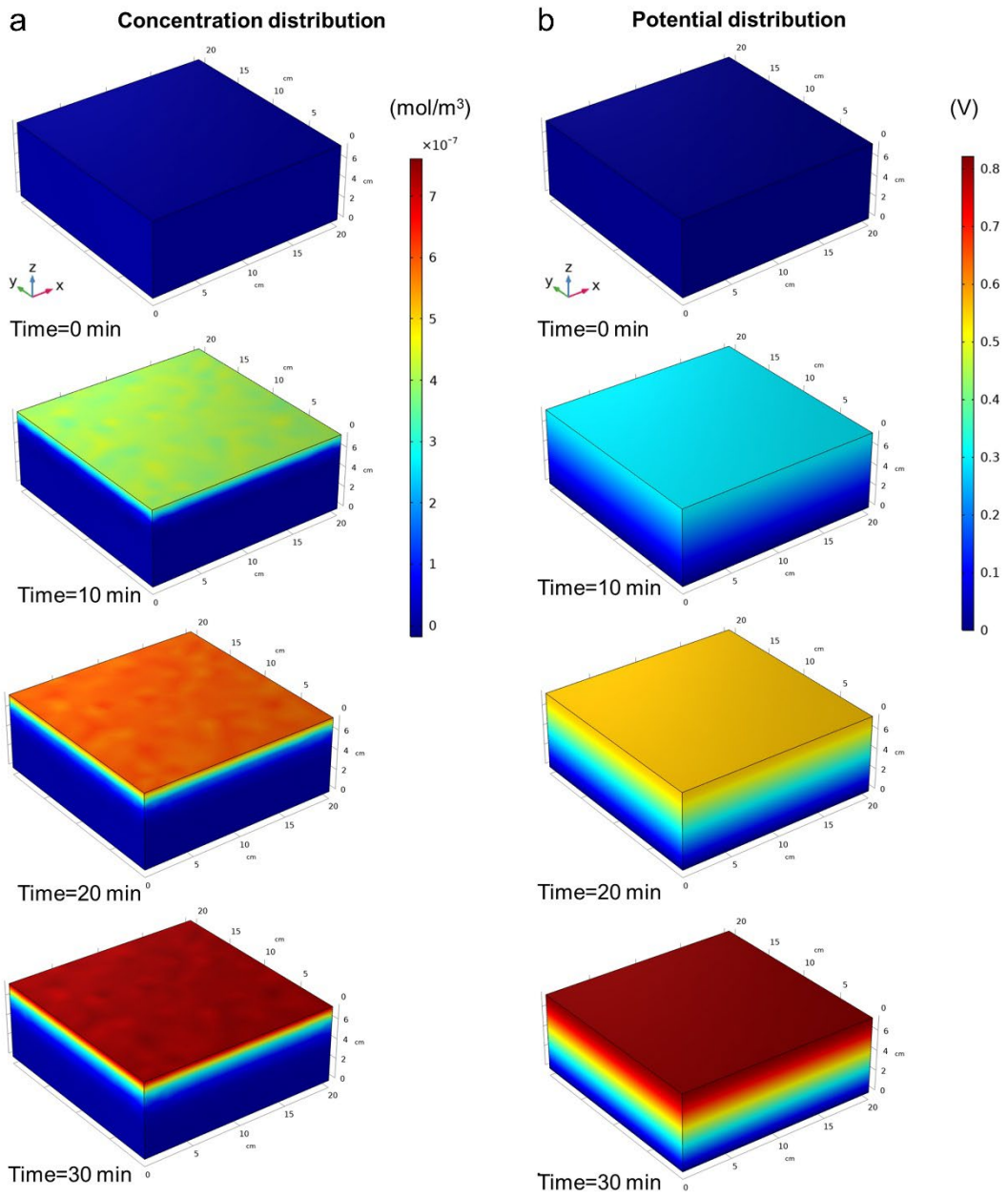


Figure S18. The simulated distribution of (a) proton concentration and (b) potential in GMS@HCDs during solar evaporation

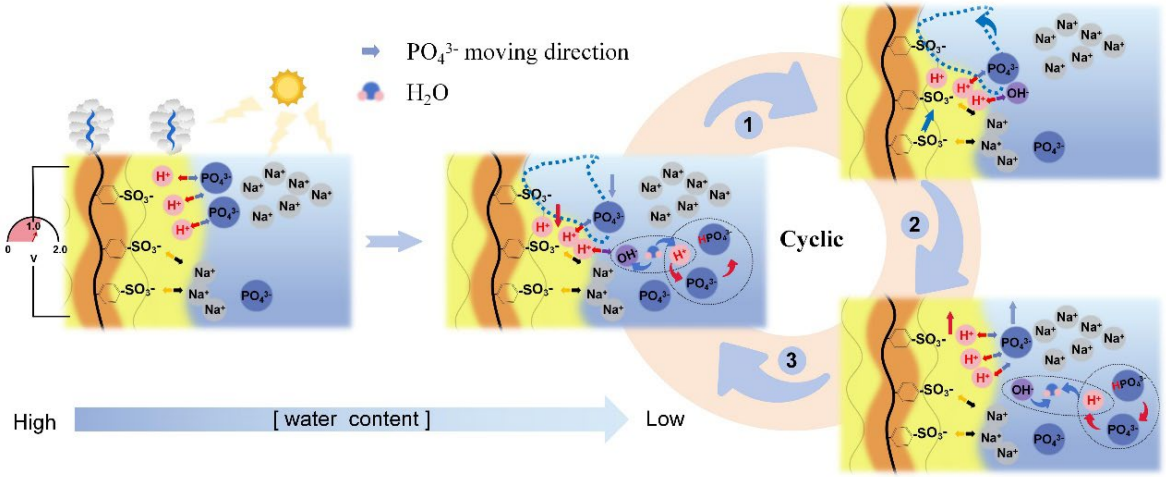


Figure S19. Schematic illustration for the influences of Na_3PO_4 solution on continuously electric generation in a GMS@HCDs

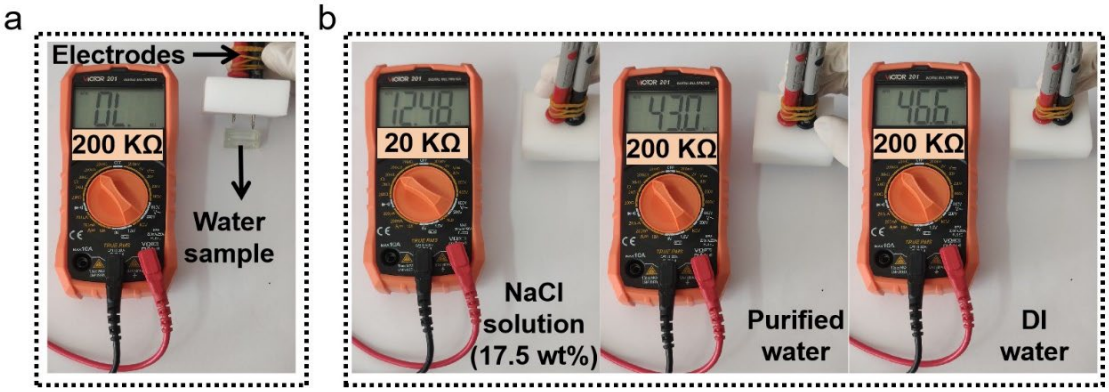


Figure S20. (a) Evaluation of water purity using a multimeter with a constant distance between electrodes; (b) The tested results demonstrating a high purity of purified water, similar to that of DI water.

3. Supporting Tables

Table S1. Comparison of the evaporation rate and solar-to-vapor efficiency of various evaporators reported previously.

NO.	Evaporator carrier	Photothermal materials	Evaporation rate (kg m^{-2} h^{-1})	Solar-to-steam conversion efficiency (%)	Ref.
1	Sponge	PEG/GO	1.32	88	[6]
2	Hydrogels	$BiVO_4$+rGO	1.6	87	[7]
3	Loofah Sponge	PAAS	1.83	94.54	[8]
4	Loofah Sponge	Co-MOF	1.93	98.5	[9]
5	Sponges	PPy+SBMA+DMSO	2.024	97.5	[10]
6	Sponge	GO+PVA	2.04	93.5	[11]
7	Sponge	CDs+starch aerogel	2.29	93.5	[12]
8	Sponge	C+PVA+AM	2.33	84.73	[13]
9	Cellulose Nanofibrils	CDs	2.5	96.45	[14]
10	Sponge	$Cu_{2-x}S$/S/rGO	2.58	95.57	[15]
11	Sponge	CDs/VAAFs	2.6	93.9	[16]
12	PU Sponge	$Fe_2(SO_4)_3$+PVP	2.8	94	[17]
13	Sponge	rGO+SA	3.13	91.54	[18]
14	HNG Gel	PPy+PVA	3.2	94	[19]
15	**Sponge+PVA +PSS**	**rGO@CDs**	**3.53**	**98.6**	**This work**

Table S2. Comparison of power generation performances for various generators

No.	Material	Form of water	Area (cm^2)	Open circuit voltage (V)	Short circuit current (μA)	Power ($mW\ m^{-2}$)	Ref.
1	LDH	Liquid Water	6	0.6	1.8	0.075	[20]
2	Carbon Black	Liquid Water	27	0.53	105.57	0.094	[21]
3	Ni-Al LDH	Liquid Water	15	0.7	19.5	0.12	[22]
4	MoS_2	Liquid Water	1	0.019	6.24	0.1932	[23]
5	Wood	Liquid Water	1	0.2016	10.2	5.14	[24]
6	Wood-WEG	Moisture	1	0.57	77	5.7	[25]
7	PSS-PVA@CDs	Moisture	1	0.83	5.2	6	[26]
8	Biofilm	Moisture	0.25	0.45	0.375	10	[27]
9	3D rGO	Liquid Water	12	0.63	609	17.4	[28]
10	Loofah Membrane	Liquid Water	1	0.2033	36	18.3	[29]
11	Microbial	Moisture	1	0.390	35.4	50.7	[30]
12	SHEs	Moisture	4	0.4	880	60	[31]
13	SiNWs	Moisture	1	0.55	22	100	[32]
14	SA-SiO_2-rGO	Moisture	0.89	0.6	97.01	120	[33]
15	Porous Carbon	Liquid Water	1	0.94	116.2	257	[34]
16	Wood +CB	Moisture	8	0.65	9600	270	[35]
17	PDMS-CNT/ CNC	Liquid Water	3.42	0.06	26000	400	[36]

18	**GMS@ HCDs**	**Liquid Water**	**4**	**0.972**	**689.52**	**943**	**This work**

References

[1] H. Sun, P. Ren, J. R. Fried, *Comput. Theor. Polym. Sci.* **1998**, *8*, 229.

[2] H. Sun, *J. Phys. Chem. B* **1998**, *102*, 7338.

[3] O. Borodin, M. Olguin, P. Ganesh, P. R. C. Kent, J. L. Allen, W. A. Henderson, *Phys. Chem. Chem. Phys.* **2016**, *18*, 164.

[4] P. B. Warren, *Phys. Rev. Lett.* **2020**, *124*, 248004.

[5] X.-S. Wang, D. He, J. J. Wylie, H. Huang, *Phys. Rev. E* **2014**, *89*, 022722.

[6] C. Liu, Y. Peng, X. Zhao, *Desalination* **2021**, *501*, 114911.

[7] L. Noureen, Z. Xie, M. Hussain, M. Li, Q. Lyu, K. Wang, L. Zhang, J. Zhu, *Sol. Energy Mater. Sol. Cells* **2021**, *222*, 110952.

[8] X. Wang, L. Zhang, D. Zheng, X. Xu, B. Bai, M. Du, *Chem. Eng. J.* **2023**, *462*, 142265.

[9] W. Ren, H. Wang, Q. Chang, N. Li, J. Yang, S. Hu, *Carbon* **2021**, *184*, 102.

[10] B. Peng, Q. Lyu, M. Li, S. Du, J. Zhu, L. Zhang, *Adv. Funct. Mater.* **2023**, *33*, 2214045.

[11] W. Lei, Y. Liu, S. Khan, N. Suzuki, C. Terashima, A. Fujishima, M. Liu, *Desalination* **2022**, *533*, 115780.

[12] X. Xu, Q. Chang, C. Xue, N. Li, H. Wang, J. Yang, S. Hu, *J. Mater. Chem. A* **2022**, *10*, 11712.

[13] A. Chu, M. Yang, H. Yang, X. Shi, J. Chen, J. Fang, Z. Wang, H. Li, *ACS Appl. Mater. Interfaces* **2022**, *14*, 36116.

[14] Y. Wang, Q. Chang, C. Xue, J. Yang, S. Hu, *J. Colloid Interface Sci.* **2022**, *621*, 33.

[15] C. Xue, Y. Shen, Q. Zhang, Q. Chang, N. Li, Y. Li, W. Zheng, S. Hu, J. Yang, *Nano Res.* **2022**, *16*, 5953.

[16] H. Zhou, C. Xue, Q. Chang, J. Yang, S. Hu, *Chem. Eng. J.* **2021**, *421*, 129822.

[17] Z. Wang, X. Wu, J. Dong, X. Yang, F. He, S. Peng, Y. Li, *Chem. Eng. J.* **2022**, *427*, 130905.

[18] J. Xu, G. Wang, L. Zhu, G. Jiang, Y. Lei, Z. Zeng, L. Xue, *Chem. Eng. J.* **2023**, *455*, 140704.

[19] F. Zhao, X. Zhou, Y. Shi, X. Qian, M. Alexander, X. Zhao, S. Mendez, R. Yang, L. Qu, G. Yu, *Nat. Nanotechnol.* **2018**, *13*, 489.

[20] J. Tian, Y. Zang, J. Sun, J. Qu, F. Gao, G. Liang, *Nano Energy* **2020**, *70*, 104502.

[21] T. G. Yun, J. Bae, A. Rothschild, I. D. Kim, *ACS Nano* **2019**, *13*, 12703.

[22] J. Sun, P. Li, J. Qu, X. Lu, Y. Xie, F. Gao, Y. Li, M. Gang, Q. Feng, H. Liang, X. Xia, C. Li, S. Xu, J. Bian, *Nano Energy* **2019**, *57*, 269.

[23] D. He, Y. Yang, Y. Zhou, J. Wan, H. Wang, X. Fan, Q. Li, H. Huang, *Nano Energy* **2021**, *81*, 105630.

[24] Q. Y. Wu, C. Wang, R. Wang, C. Chen, J. Gao, J. Dai, D. Liu, Z. Lin, L. Hu, *Adv. Energy Mater.* **2019**, *10*, 1902590.

[25] T. Cai, L. Lan, B. Peng, C. Zhang, S. Dai, C. Zhang, J. Ping, Y. Ying, *Nano Lett.* **2022**, *22*, 6476.

[26] Z. Yan, N. Li, Q. Chang, C. Xue, J. Yang, S. Hu, *Chem. Eng. J.* **2023**, *467*, 143443.

[27] X. Liu, T. Ueki, H. Gao, T. L. Woodard, K. P. Nevin, T. Fu, S. Fu, L. Sun, D. R. Lovley, J. Yao, *Nat. Commun.* **2022**, *13*, 4369.

[28] G. Zhang, Z. Duan, X. Qi, Y. Xu, L. Li, W. Ma, H. Zhang, C. Liu, W. Yao, *Carbon* **2019**, *148*, 8.

[29] P. Luan, Y. Zhao, Q. Li, D. Cao, Y. Wang, X. Sun, C. Liu, H. Zhu, *Small* **2022**, *18*, 2104320.

[30] G. Ren, Q. Hu, J. Ye, X. Liu, S. Zhou, Z. He, *Chem. Eng. J.* **2022**, *441*, 135921.

[31] H. Wang, Y. Sun, T. He, Y. Huang, H. Cheng, C. Li, D. Xie, P. Yang, Y. Zhang, L. Qu, *Nat. Nanotechnol.* **2021**, *16*, 811.

[32] B. Shao, Z. Song, X. Chen, Y. Wu, Y. Li, C. Song, F. Yang, T. Song, Y. Wang, S. T. Lee, B. Sun, *ACS Nano* **2021**, *15*, 7472.

[33] H. Wang, T. He, X. Hao, Y. Huang, H. Yao, F. Liu, H. Cheng, L. Qu, *Nat. Commun.* **2022**, *13*, 2524.

[34] K. Liu, T. Ding, J. Li, Q. Chen, G. Xue, P. Yang, M. Xu, Z. L. Wang, J. Zhou, *Adv. Energy Mater.* **2018**, *8*, 1702481.

[35] T. Chen, D. Zhang, X. Tian, S. Qiang, C. Sun, L. Dai, M. Zhang, Y. Ni, X. Jiang, *Carbohydr. Polym.* **2022**, *294*, 119809.

[36] L. Zhu, T. Ding, M. Gao, C. K. N. Peh, G. W. Ho, *Adv. Energy Mater.* **2019**, *9*, 1900250.